



Tropical oceanic intraseasonal variabilities associated with central Indian Ocean mode

Ze Meng¹ · Lei Zhou^{1,2} · Raghu Murtugudde³ · Qingxuan Yang^{4,5} · Kandaga Pujiana⁶ · Jingyuan Xi⁷

Received: 9 October 2020 / Accepted: 1 September 2021 / Published online: 22 September 2021
© The Author(s), under exclusive licence to Springer-Verlag GmbH Germany, part of Springer Nature 2021

Abstract

The oceanic intraseasonal variabilities (ISVs) are pronounced over the tropical Indian Ocean. Recently, a Central Indian Ocean (CIO) mode was proposed as an ocean–atmosphere coupled mode at intraseasonal timescales. It has a close relation with northward-propagating ISVs and intraseasonal precipitation during the Indian summer monsoon. In this study, the dynamics of tropical oceanic ISVs associated with the CIO mode are analyzed using reanalysis products and observations. A complete heat budget analysis shows that intraseasonal SST anomalies which propagate westward from the eastern to the central tropical Indian Ocean during the CIO mode are mainly attributable to zonal thermal advection. Surface heat flux is the second largest contributor. This is distinct from the traditional tropical oceanic ISVs as a response to the Madden–Julian Oscillation (MJO) in the atmosphere, in which surface heat flux is usually the dominant component. Current results along with the previously reported atmosphere dynamics during the CIO mode depict a framework for the ocean–atmosphere coupled mode over the tropical Indian Ocean. This represents a more comprehensive understanding of tropical ISVs and will ultimately contribute to the improvement in process understanding, simulations, and forecasts of the Indian summer monsoon.

Keywords Oceanic intraseasonal variability · Tropical Indian Ocean · Mixed layer heat budget · Ocean circulation

1 Introduction

Intraseasonal variabilities (ISVs) with a period of 30–60 days are pronounced over the tropical Indian Ocean. Sea surface temperature (SST) anomalies during an intraseasonal event can be as large as 1 °C while the composite intraseasonal SST anomalies tend to be around 0.3 °C (Schott et al. 2009; Shinoda et al. 1998). The ISVs in ocean currents can overwhelm their seasonal and interannual counterparts, such as the Wyrтки jet (Masumoto et al. 2005; Wyrтки 1973). It has been shown that the oceanic ISVs play an important role in both weather and climate over the Indo-Pacific region. Particularly, SST anomalies over the tropical Indian Ocean are critical for northward-propagating ISVs during the Indian summer monsoon [commonly known as the monsoon intraseasonal oscillation (MISO); Goswami 2005; Waliser 2006], which bring abundant moisture and momentum from the tropics to the subtropics. Therefore, a better understanding of the dynamics of oceanic ISVs over tropical Indian Ocean is of significant scientific importance and will eventually help to improve Indian monsoon simulations and forecasts which are still a grand scientific challenge (Hurley and Boos 2013; Wang et al. 2005).

✉ Lei Zhou
zhoulei1588@sjtu.edu.cn

- ¹ School of Oceanography, Shanghai Jiao Tong University, Shanghai, China
- ² Southern Marine Science and Engineering Guangdong Laboratory (Zhuhai), Zhuhai, China
- ³ University of Maryland, College Park, MD, USA
- ⁴ Physical Oceanography Laboratory/Institute for Advanced Ocean Study/Sanya Oceanographic Institution, Ocean University of China, Qingdao/Sanya, China
- ⁵ Pilot National Laboratory for Marine Science and Technology (Qingdao), Qingdao, China
- ⁶ Cooperative Institute for Marine and Atmospheric Studies and NOAA Atlantic Oceanographic and Meteorological Laboratory, Miami, USA
- ⁷ State Key Laboratory of Satellite Ocean Environment Dynamics, Second Institute of Oceanography, Ministry of Natural Resources, Hangzhou, China

Most studies on oceanic ISVs focus on the oceanic response to the Madden–Julian Oscillation (MJO), which is a major component of ISVs in the atmosphere (e.g., Jin et al. 2012, 2013; Waliser et al. 2003, 2004). From observational experiments like Coupled Ocean–Atmosphere Response Experiment (COARE), SST and the mixed layer depth (MLD) show a clear eastward propagation along with the MJO (Hendon and Glick 1997). As a result, the eastward propagating oceanic ISVs within the tropical regions are now widely studied and are assessed in model simulations of ISVs (Li et al. 2016). However, a Central Indian Ocean (CIO) mode was proposed by Zhou et al. (2017b), whose mechanisms and the associated oceanic ISVs are fundamentally different from those during MJO. Thus, the motivation of this study is to present the comprehensive dynamics and thermodynamics of the oceanic ISVs associated with the CIO mode in the tropical Indian Ocean. This is also essential for completing the picture of the CIO mode, which has already been established as a coupled ISV mode in several studies cited below.

The CIO mode is defined as the first combined Empirical Orthogonal Function (EOF) mode of the intraseasonal SST anomalies and intraseasonal zonal wind anomalies at 850 hPa (referred to as U850 hereafter) within 40°–120°E and 20°N–20°S (Zhou et al. 2017b). The principal component of the first combined EOF is defined as the CIO mode index (red curves in Fig. 1b–d), which indicates the strength of the CIO mode. During its positive phase, warm intraseasonal SST anomalies and an anticyclonic gyre at 850 hPa coherently occur over the tropical Indian Ocean (Fig. 1a). Such ocean–atmosphere coupling over the central Indian Ocean generates a vertical wind shear of zonal winds (Jiang et al. 2004; Kang et al. 2010), and hence favors the northward propagation of MISO (Zhou et al. 2017b) from the equator to the northern Bay of Bengal (BoB). Hence, the CIO mode has a close relation with the northward-propagating MISO, and the CIO mode is the tropical coupled origin of MISO. As expected, the CIO mode index has a high correlation (up to 0.8) with the intraseasonal rainfall over the Indian summer monsoon region (Zhou et al. 2017a). In addition, the CIO mode is clearly distinct from the MJO. It should be noted upfront that the CIO mode and the MJO occur predominantly in different seasons. The peaks of the CIO mode index, which are larger than the standard deviation (STD) of the index, are marked with red dots in Fig. 1b–d. The MJO is represented with the Real-time Multivariate (RMM) index (Wheeler and Hendon 2004). The negative RMM2 index represents the MJO convective center over the tropical Indian Ocean, and thus only RMM2 is shown for clarity with blue lines in Fig. 1b–d. The peaks of RMM2, which are larger than the STD of RMM2, are marked with blue dots. During the Indian summer monsoon (June to September) from 1992 to 2019, there are 129 peaks

in the CIO mode index and 208 peaks in RMM2. Only 9 peaks in the CIO mode index and RMM2 are the same. The correlation between the CIO mode index and RMM2 is only 0.35, which is not statistically significant at a confidence level of 95%. Therefore, the peaks of the CIO mode are on different days from those of RMM2 during boreal summer. The same conclusion can be obtained by comparing the CIO mode index and RMM1 (not shown; Li et al. 2020). Secondly, the vertical structure in the atmosphere and the major energy source of the CIO mode and MJO are also distinct. The former is dominated by a barotropic structure and a barotropic energy conversion from the horizontal shear of the background winds (Zhou et al. 2018). In contrast, MJO is dominated by a baroclinic structure (Jiang et al. 2015; Kiladis et al. 2005; Wallace and Adames 2014) and a baroclinic energy gain from the available potential energy (Zhou et al. 2012). Overall, the CIO mode is *prima facie* independent of MJO, and hence the following diagnoses shed new insights to broaden our understanding of the oceanic ISVs during boreal summer in the tropical Indian Ocean.

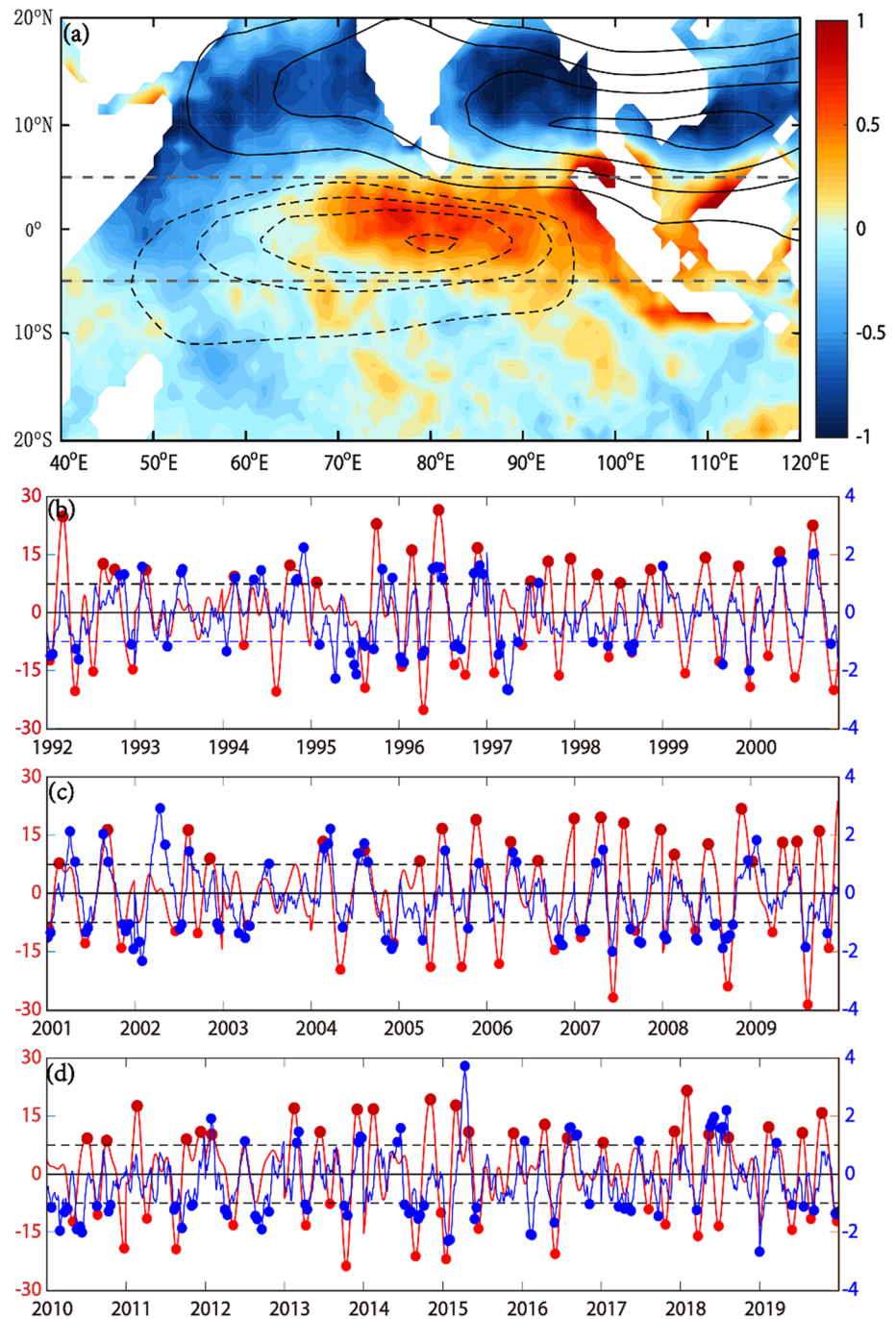
In this study, we focus on the intraseasonal SST anomalies over the tropical Indian Ocean. The mechanisms are explored mainly via a comprehensive mixed layer heat budget, which is indispensable for a complete understanding of the thermal effects and ocean dynamics studies (e.g., de Szoeke et al. 2015; Stevenson and Niiler 1983). The rest of this paper is organized as follows. Data and methods are introduced in Sect. 2. The distinctions of oceanic ISVs associated with the CIO mode are presented in Sect. 3. The heat budget analysis for the upper mixed layer is conducted and the mechanisms are summarized in Sect. 4. Conclusions and discussion are presented in Sect. 5.

2 Data and methods

2.1 Data

SST data are obtained from the NOAA 1/4° daily Optimum Interpolation SST (OISST; Reynolds et al. 2007). Other oceanic variables, such as ocean currents and temperatures are obtained from the reanalysis ECCO2 (Estimating the Circulation and Climate and the Ocean, Phase II; Menemenlis et al. 2005). The horizontal resolution of ECCO2 is 0.25° latitude × 0.25° longitude. There are 50 levels in the vertical. In upper 120 m, there are 12 layers and the vertical interval is about 10 m. ECCO2 has daily outputs for all two-dimensional variables (such as SST and net surface heat flux) and 3-day outputs for all three-dimensional variables (such as ocean currents). All 3-day outputs in ECCO2 are interpolated into daily values. It is verified that the following results do not change significantly due to the interpolation (not shown). The ECCO2 products from 1992 to 2019 are used

Fig. 1 a The CIO mode obtained from OISST intraseasonal SST anomalies (colors) and NCEP-NCAR reanalysis intraseasonal zonal wind anomalies at 850 hPa (dashed contours). Both SST and zonal winds are daily averages from 1992 to 2019. All modes are normalized, so that the maximum magnitude of the SST mode is 1. **b–d** The daily CIO mode index (red lines) and RMM2 index (blue lines) during the Indian summer monsoon (from June to September) from 1992 to 2019. The black dashed lines denote the thresholds (one standard deviation) for the positive and negative phases of the CIO mode. Significant CIO mode peaks are marked with red dots and MJO peaks are marked with blue dots. Positive red dots are referred as Day 0 for the composites in Figs. 3 and 5



for analysis here. There are other reanalysis products which are also able to resolve the oceanic ISVs; for ex., the Simple Ocean Data Assimilation (SODA; Carton and Giese 2008), which has a 5-day interval for all variables. The simulated ISVs in different reanalysis products were compared and it was found that ECCO2 has stronger and more realistic ISVs than SODA and the other reanalysis products, especially in the ocean interior (Zhang et al. 2016). Therefore, ECCO2 is the best choice among all available reanalysis products for the analyses in this study. The daily net surface heat flux is

obtained from the Air-Sea Fluxes for the Global Tropical Oceans (TropFlux; Kumar et al. 2012), and the daily sea surface wind stress is obtained from NOAA multi-satellite blended sea surface wind stress (Zhang et al. 2006). All intraseasonal variables are obtained with a 20-to-100-day Butterworth band-pass filter. To eliminate the influence of high autocorrelation in band-pass filtered records, the effective sample sizes are calculated according to Bretherton et al. (1999) for the significance test on correlation coefficients.

In addition, data from RAMA arrays (Research Moored Array for African-Asian-Australian Monsoon Analysis; McPhaden et al. 2009) and Argo profiles (Array for Real-time Geostrophic Oceanography; Argo 2000) are also used to validate the effects of temperature advection (see Sect. 4.3 for more details). Three buoys in the RAMA array in the central equatorial Indian Ocean are included. They are all deployed at 90°E and their latitudes are at the equator, 1.5°N, and 1.5°S, respectively. All three buoys have vertical profiles of temperatures, while only the one at the equator has a vertical profile of ocean currents. In order to estimate the temperature advection in the upper mixed layer, mainly the daily data from the buoy at (0°, 90°E) are used below. Raw temperatures and ocean current profiles are shown in Fig. 2a, b. The missing data in both temperature and ocean currents are processed as follows, in order to facilitate the isolation of ISVs using a band-pass filter. First, the missing data are replaced with the mean value of temperatures from buoys at (1.5°N, 90°E) and (1.5°S, 90°E) at the same time and the same depth, if there are data at these two off-equatorial buoys. Second, the remaining missing data are filled using a linear interpolation (Fig. 2c). For ocean currents, since there are no vertical profiles at the two buoys at

1.5°N and 1.5°S, the missing data are just filled using a linear interpolation (Fig. 2d). Since there are no measurements of ocean currents for 2009 and 2015, and no measurements of temperature for 2015 and 2016, the data gaps are maintained (blank areas in Figs. 2c, 12d). Then, the ISVs in temperature and ocean current are obtained from the daily interpolated data using a band-pass filter (Fig. 2e, f). The Argo profiles near the RAMA array at (0°, 90°E) and the record lengths of the Argo profiles are long enough (longer than 100 days) to isolate the ISVs are also used. Since the location of an Argo float changes constantly, the location of each Argo float is rounded to the nearest regular grid with a resolution of 2° latitude × 2° longitude.

2.2 Heat budget for the upper ocean mixed layer

The thermodynamic equation for the upper mixed layer can be written as

$$\frac{\partial \langle T \rangle}{\partial t} = H_{adv} + V_{adv} + Ent + \frac{Q}{\rho C_p h} + \langle R_H \rangle, \quad (1)$$

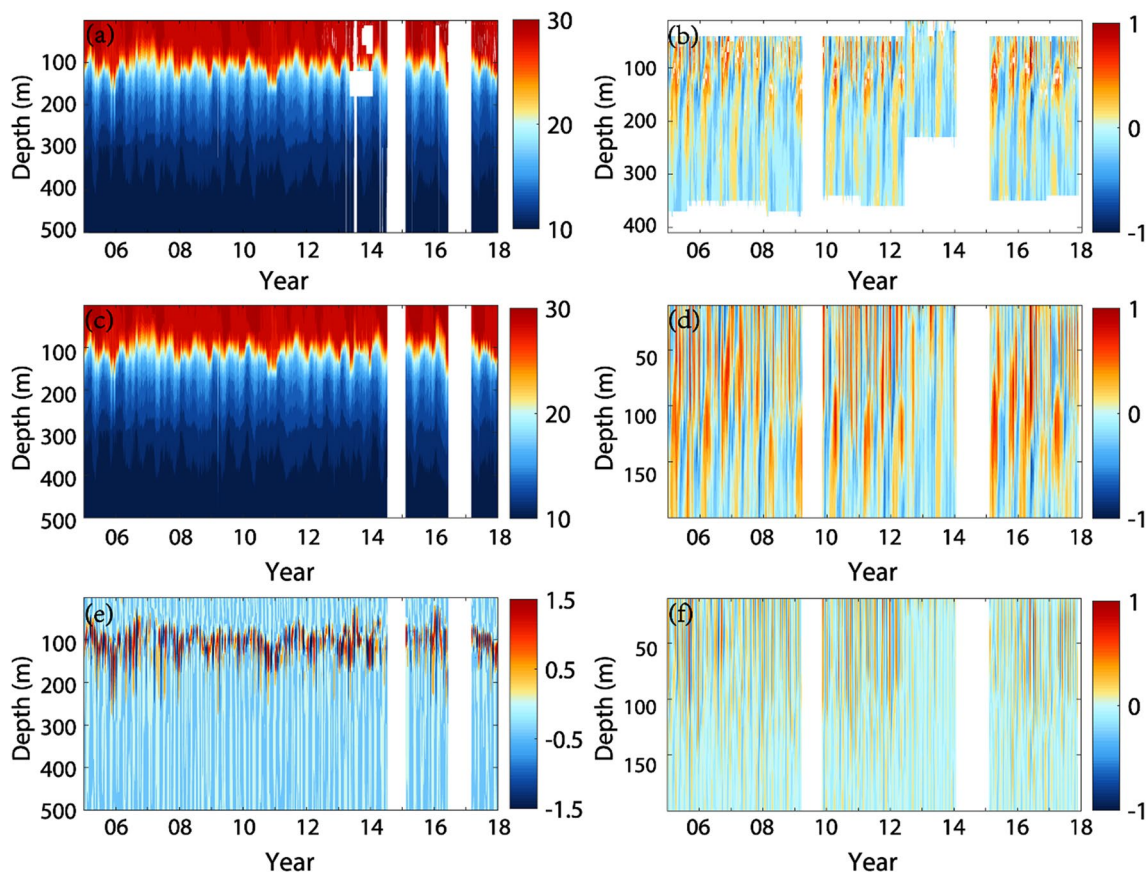


Fig. 2 Temperatures (left column) and zonal currents (right column) from the RAMA buoy at (0°, 90°E). **a, b** are the raw data. **c, d** are the data after the missing data being replaced and the linear interpolation

being executed. See main text for details of the replacement and interpolation. **e, f** are ISVs obtained with a band-pass filter. The unit for temperature is °C and the unit for zonal current is m/s

where T is the temperature; $\langle \cdot \rangle = \frac{1}{h} \int_{-h}^0 \cdot dz$ denotes the vertical mean within the mixed layer, h is the surface mixed layer depth (MLD) which is a function of both space and time; $H_{adv} = -\langle \vec{U}_H \cdot \nabla_H T \rangle$ is horizontal advection; $V_{adv} = -\langle w \frac{\partial T}{\partial z} \rangle$ represents vertical advection; $Ent = \frac{1}{h} \frac{\partial h}{\partial t} (T|_{z=-h} - \langle T \rangle)$ represents entrainment; $\vec{U}_H = \vec{u}i + \vec{v}j$ is the horizontal ocean current vector, \vec{i} and \vec{j} are the unit vectors in the eastward and northward directions, respectively; $\nabla_H = \frac{\partial}{\partial x} \vec{i} + \frac{\partial}{\partial y} \vec{j}$; $Q = Q_{surf} - Q_{-h}$ denotes the net heat gain by the mixed layer, Q_{surf} is the net surface heat flux, $Q_{-h} = Q_{sw} [Re^{-\frac{h}{\gamma_1}} + (1 - R)e^{-\frac{h}{\gamma_2}}]$, $R = 0.62$, $\gamma_1 = 1.5m$ and $\gamma_2 = 20m$ are attenuation depths. Here, Q_{sw} is shortwave radiation and h is the MLD (Paulson and Simpson 1977; Qu 2003); $C_p = 4096 J/(kg \cdot ^\circ C)$ is the heat capacity; $\rho = 1.025 \times 10^3 kg/m^3$ is the sea water density; and R_H is the residual term. R_H also includes analysis increments that are unbalanced within the reanalysis data as well as the other implicit budget terms such as mixing and diffusivity. In this study, the MLD is defined as the depth where temperature is lower than that at 10 m by 0.8 °C, following Kara et al. (2000), which was verified to have a good accuracy for data with a low vertical resolution. The barrier layer is estimated following Drushka et al. (2014) and Qu and Meyers (2005). Results show that the barrier layer is thin (less than 10 m) and the associated influences can be omitted. MLD can also be estimated with other methods, such as the one that relies on seawater density following Monterey and Levitus (1997), but the results are qualitatively the same. The central difference scheme is applied for the horizontal gradient computations ($\partial/\partial x$ and $\partial/\partial y$), with Δx and Δy of 0.25° longitude and 0.25° latitude, respectively, which are the horizontal resolutions of ECCO2. The derivations are presented in detail in the Appendix.

All variables can be decomposed into two scales. One is the low-frequency or the background component which has a period longer than 100 days. The other is the perturbation or the intraseasonal component with a period between 20 and 100 days. The background component is denoted with an overbar and the intraseasonal component is denoted with a prime, for example, $T = \bar{T} + T'$. The high-frequency components with a period shorter than 20 days can also be included in the decomposition (Zhou et al. 2012). However, none of the components containing the high-frequency variabilities are found to be large enough. Therefore, the high-frequency variabilities are ignored hereafter. Neglecting all terms that contain a product of two or more perturbation variables, the intraseasonal component of Eq. (1) becomes

$$\frac{\partial \langle T' \rangle}{\partial t} = adv \bar{U} T' + adv U' \bar{T} + V'_{adv} + Ent' + \frac{Q'}{\rho C_p \bar{h}} + \langle R_H \rangle', \tag{2}$$

where $adv \bar{U} T' = -\langle \bar{u} \frac{\partial T'}{\partial x} \rangle - \langle \bar{v} \frac{\partial T'}{\partial y} \rangle$ represents the intraseasonal temperature anomaly advected by the background currents, $adv U' \bar{T} = -\langle u' \frac{\partial \bar{T}}{\partial x} \rangle - \langle v' \frac{\partial \bar{T}}{\partial y} \rangle$ represents the mean temperature advected by the intraseasonal currents.

Besides ECCO2, the heat budget terms in Eq. (2) are also estimated using *in-situ* data in Sect. 4.3. For advection, taking $-\langle u' \frac{\partial \bar{T}}{\partial x} \rangle$ for example, u' is the intraseasonal zonal current obtained from the RAMA array; $\frac{\partial \bar{T}}{\partial x} \approx \frac{\bar{T}_{Argo} - \bar{T}_{RAMA}}{x_{Argo} - x_{RAMA}}$ where \bar{T}_{Argo} and \bar{T}_{RAMA} are the background temperatures obtained from Argo float and RAMA array, x_{Argo} and x_{RAMA} are longitudes of Argo float and RAMA array, respectively; the vertical mean over the MLD (angle brackets) are calculated using the vertical profiles of $u' \frac{\partial \bar{T}}{\partial x}$; MLD is calculated in the same way as that in ECCO2. The term $\frac{Q'}{\rho C_p \bar{h}}$ is also estimated by $Q' = \left(Q_{surf} - Q_{sw} \left[Re^{-\frac{h}{\gamma_1}} + (1 - R)e^{-\frac{h}{\gamma_2}} \right] \right)'$, in which Q_{surf} and Q_{sw} come from TropFlux, ρ and \bar{h} from the RAMA array at (0°, 90°E). All other terms are estimated in a similar way.

3 Tropical oceanic ISVs associated with CIO mode

In this section, the two distinct and specific differences in oceanic ISVs between the MJO and the CIO mode are discussed, i.e.,

- (1) Intraseasonal SST anomalies associated with the CIO mode propagate westward in tropics;
- (2) Net surface heat flux forcing is not the dominant mechanism for these westward propagating intraseasonal SST variabilities in tropics.

With respect to the positive peak days of the CIO mode index which is larger than its STD (the days marked with red dots in Fig. 1b–d, also referred as Day 0 in Figs. 3 and 5), the composite intraseasonal SST anomalies (obtained from OISST; colors in Fig. 3) averaged between 2°N and 2°S propagate westward from 100°E to 70°E, which is opposite to the direction of either equatorial Kelvin waves in the ocean or the MJOs in the atmosphere. The westward propagation can be further estimated by the “centroid” of SST anomalies at each longitude. Taking the warm SST anomalies from Day – 10 to Day 10 as an example, the “centroid” at each longitude is calculated as

$$t_c = \frac{\sum t_i \cdot SST_i}{\sum SST_i}, \tag{3}$$

where t_c stands for time. The westward propagation of the “centroids” (t_c ; white crosses in Fig. 3) can be clearly

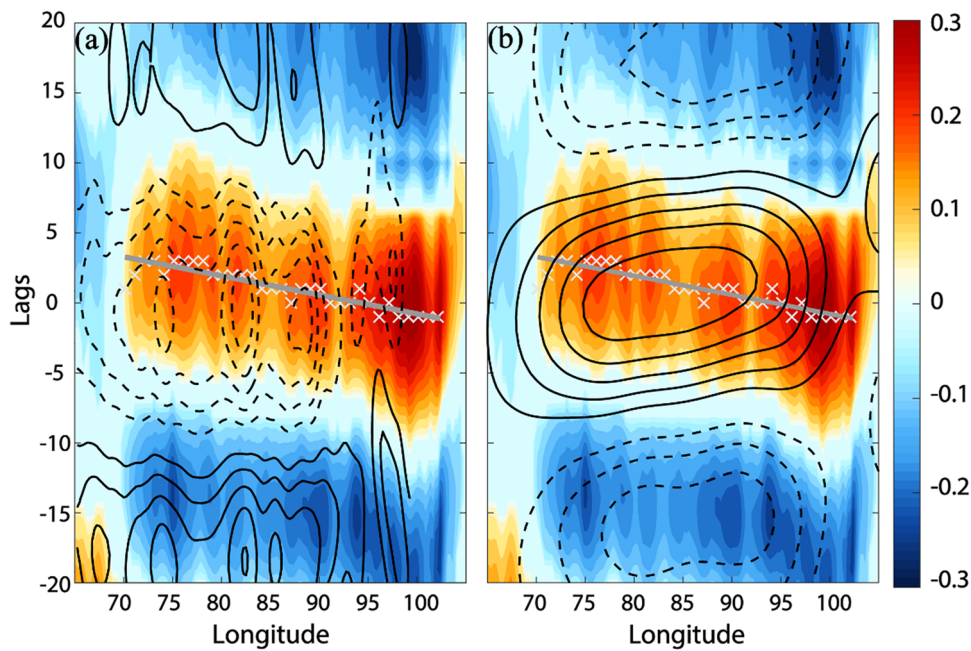


Fig. 3 **a** Composite Hovmöller diagrams of intraseasonal SST anomalies (colors; obtained from OISST; the unit is °C) and surface wind stress (contours; the units is N/m²). The composites are averaged between 2°N to 2°S. Surface wind stresses are from -0.06 to 0.06 N m⁻² with an interval of 0.01 N m⁻². Solid contours are for westerly wind stresses and dashed contours are for easterly wind stresses. The white crosses are the “centroid” of warm SST anomalies

at each longitude calculated with Eq. (3). The gray line is the least square fit and the slope is ~-0.15 day/degree. **b** Is the same as **(a)**, but the contours are for the intraseasonal net surface heat flux Q'_{surf} (contours; obtained from TropFlux) from -25 to -5 W/m² (dashed contours) and from 5 to 25 W/m² (solid contours) with an interval of 5 W/m²

seen with the least-squares fit (dark gray line in Fig. 3). The westward speed is around 0.15 degree/day (8.5 m/s). The westward propagation is also discernible if the average is taken between 5°N and 5°S (not shown), where the intraseasonal SST anomalies are pronounced (Fig. 1a).

Remarkably, the westward propagation between 2°N and 2°S is not attributable to Rossby waves. As shown with the wavenumber-frequency spectrum of oceanic equatorial waves following the procedure described in Farrar and Durland (2012), the signals of free Rossby waves are not clear

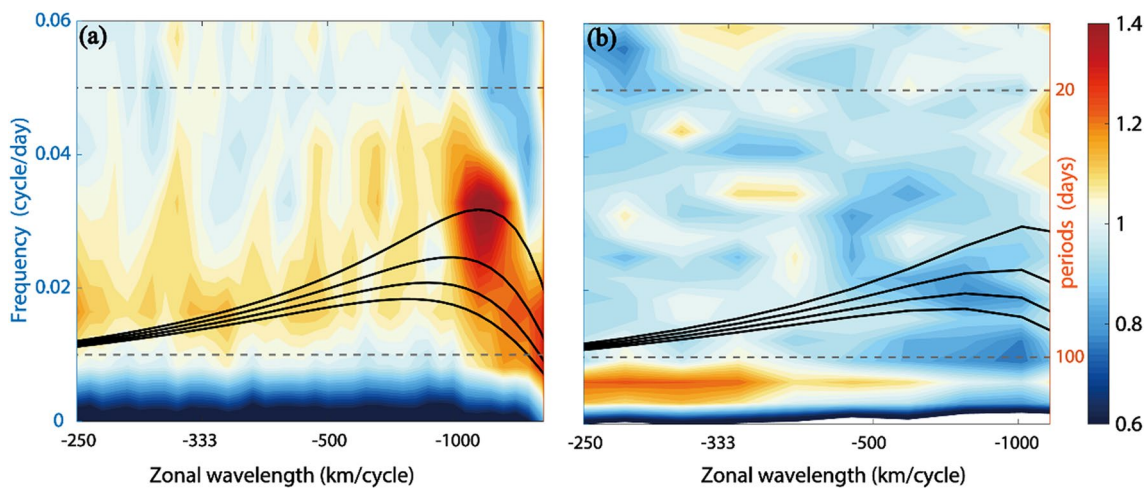


Fig. 4 Wavenumber-frequency spectra of the symmetric component of SST from OISST in the **a** equatorial Pacific Ocean (160°E–70°W, 10°N–10°S) and **b** equatorial Indian Ocean (70°E–96°E, 2°N–2°S).

Negative zonal wavelength denotes the signals with a westward propagation. Black curves are the first baroclinic mode of free Rossby waves for the first 4 meridional modes

within the equatorial Indian Ocean (70°E–96°E, 2°N–2°S) in Fig. 4b (Nagura and McPhaden 2010; Qiu et al. 1997). Moreover, the propagation speed of SST anomalies (8.5 m/s in Fig. 3) is much faster than the free Rossby waves. The annual cycle of SST also propagates eastward in the equatorial Indian Ocean in contrast to the westward propagation in the equatorial Pacific and Atlantic oceans (Murtugudde and Busalacchi 1999). The Rossby waves are rather obvious in the equatorial Pacific Ocean (160°E–70°W, 10°N–10°S) as shown in Fig. 4a, which are consistent with the results in Delcroix et al. (1991), Shinoda et al. (2009), Wakata (2007), and many others. Although there are no free Rossby waves in intraseasonal SST variability in the equatorial Indian Ocean, intraseasonal surface wind stress anomalies (obtained from the NOAA multi-satellite blended sea surface wind stress) propagate westward during the CIO mode (contours in Fig. 3a) and lead the intraseasonal SST anomalies by ~5 days. It can be hypothesized that the westward propagation of intraseasonal SST anomalies during the CIO mode is closely related to the surface wind stress (see more discussion below).

The composite net surface heat flux (obtained from TropFlux; contours in Fig. 3b) is not fully consistent with the SST variabilities (colors in Fig. 3b). For example, the net surface heat flux propagates eastward, which is opposite to the westward propagation of the SST anomalies. This indicates that the air-sea heat flux alone cannot explain the intraseasonal SST anomalies. Qualitatively same results can be obtained with other heat flux datasets, such as the OAFflux (Objectively Analyzed air-sea Fluxes, Weller and Yu 2007; not shown). Quantitatively, the contribution of net surface heat flux to the SST tendency is evaluated using a one-dimensional thermodynamic equation (Hendon 2003),

$$\frac{\partial \langle T \rangle'}{\partial t} = \frac{Q'}{\rho C_p \bar{h}}, \tag{4}$$

where all variables follow the definitions in Eq. (2). Obviously, Eq. (4) is a truncated version of Eq. (2) by neglecting all ocean dynamics terms. For the composite CIO mode with respect to the positive red dots (Day 0) in Fig. 1b–d, Eq. (4) is initiated on Day –30 and integrated forward every day. $Q = Q_{surf} - Q_{-h}$ is as defined in Eq. (2) and can be calculated with daily TropFlux, $\rho = 1.025 \text{ g/cm}^3$, and the mean MLD, \bar{h} is from the climatological Argo data (Holte et al. 2017). The regional-mean composite variation of intraseasonal SST anomalies (from OISST) from Day -30 onward (averaged within 70°E–100°E and 2°N–2°S) are shown with a solid line in Fig. 5. Corresponding daily integrated SST anomalies using Eq. (4) are superimposed with a dashed line. The correlation coefficient between the observed and the integrated intraseasonal SST anomalies is 0.58, which indicates that Q' only explains about 30% variance of intraseasonal SST

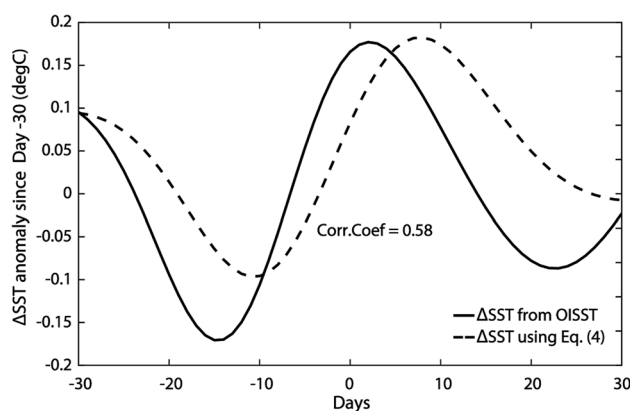


Fig. 5 Solid line: Composite intraseasonal SST anomalies averaged within 70°E–100°E and 2°N–2°S. Dashed line: SST anomalies integrated daily from Day –30 following Eq. (4). The reference days (Day 0) for the composite are the days marked with red circles in Fig. 1b–d. The correlation coefficient between the two lines is 0.58

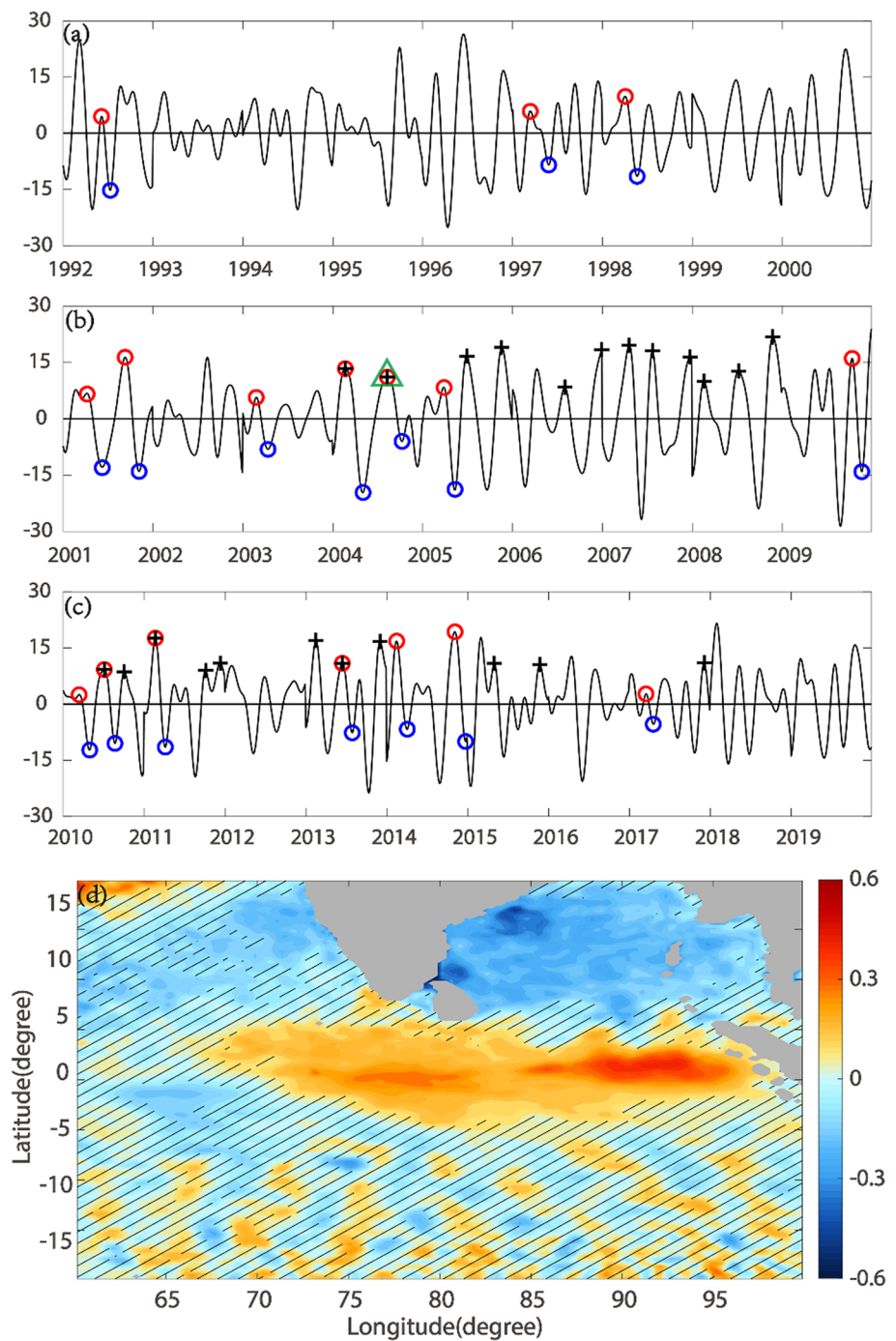
anomalies during the CIO mode. Various regions and time periods are tested for the regional mean in Fig. 5, and the results remain consistent and robust. Therefore, Q' , while still important for the SST variabilities during the CIO mode, does not play a dominant role. Moreover, using data from the cooperative Indian Ocean experiment on intraseasonal variability in the Year 2011 (CINDY2011), Seiki et al. (2013) also reported that the surface heat flux could not account for the intraseasonal SST anomalies over the tropical Indian Ocean. The fact that Q' does not dominate the SST variabilities is different from the traditional understanding in the oceanic ISVs as a response to MJOs. Therefore, besides Q' , other contributions need to be considered for tropical Indian Ocean ISVs during the CIO mode.

4 Mechanism for tropical oceanic ISVs during CIO mode

4.1 Westward-propagating intraseasonal SST anomalies in ECCO2

The intraseasonal SST anomalies over the tropical Indian Ocean and their westward propagation (from 100°E to 70°E in Fig. 3) during the Indian summer monsoon are a distinct feature associated with the CIO mode. In ECCO2, composite Hovmöller diagram of intraseasonal SST anomalies with respect to the actual CIO mode index (red curves in Fig. 1b–d) has a similar pattern to Fig. 3 (not shown). However, due to initializations and the quality of reanalysis products, a day-to-day match between ECCO2 and observations cannot be expected. In order to capture the westward propagation of intraseasonal SST anomalies during the CIO mode in ECCO2, all significant positive peaks during the

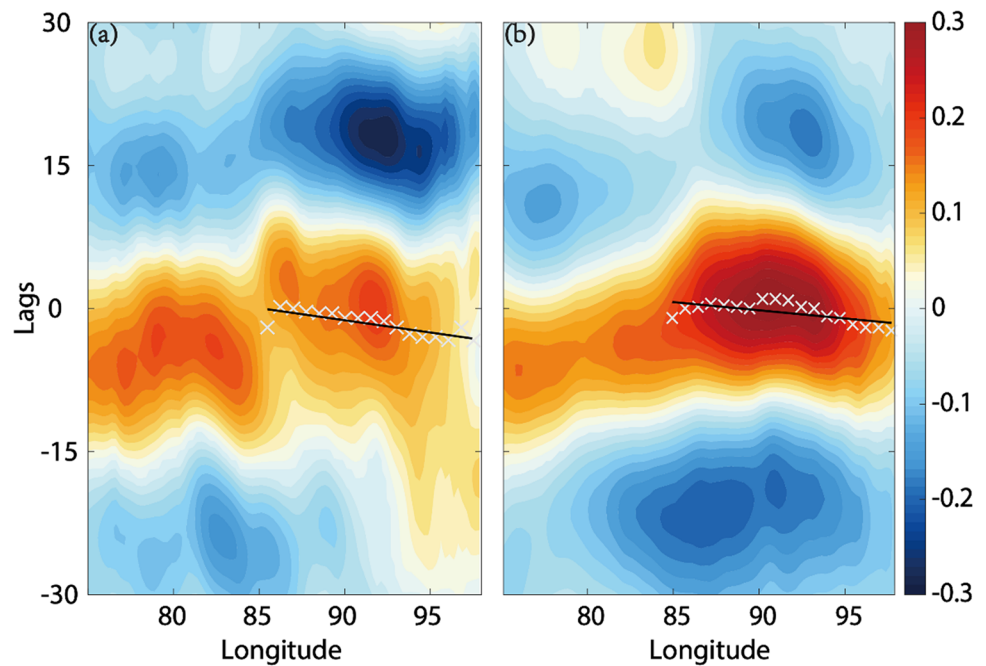
Fig. 6 **a–c** Black curves are the same CIO mode index as red curves in Fig. 1b–d, but the red circles mark the selected CIO mode peaks with westward propagation of SST anomalies in ECCO2. The blue circles are the following days with a minimal SST anomaly. See the main text for more details about the selection of the days marked with circles. The peaks marked with black plus are the days listed in Table 1 and used in Figs. 13, 14, 15. The green triangle in **b** is the CIO mode positive peak on Aug. 22nd, 2004 and used as an example for westward SST propagation in ECCO2 (Fig. 7a). **d** Differences of the intraseasonal SST anomalies between the peak days (marked with red circles) and the trough days (marked with blue circles) in **a–c**. The unit is °C. The differences covered with slashes in **(d)** are not statistically significant from null at a 95% confidence level



Indian summer monsoon (from June to September) from the observed CIO mode index (black curves lines in Fig. 6a–c) are taken into consideration. The CIO mode events are chosen as the ones with westward propagation of intraseasonal SST anomalies from ECCO2 (red dots in Fig. 6a–c). Same as in Fig. 3, for 10 days before and 10 days after each peak in the CIO mode index, the “centroids” of warm SST anomalies are calculated at each longitude and a linear fit is applied to the scattered “centroids”. If the westward propagation speed of the SST anomalies is within 0.1 to 0.2 days/degree,

this peak is selected as Day 0 for the following composite analysis and marked with a red circle in Fig. 6a–c. For each Day 0, the following days with a minimal SST anomaly are marked with blue circles in Fig. 6a–c. The red and blue circles delineate the range of an intraseasonal event. There are 17 intraseasonal events selected using this empirical procedure from ECCO2 during 1992 to 2019. These events are then used as reference for the following composite analysis (Figs. 6, 7, 8, 9, 10, 11).

Fig. 7 Composite Hovmöller diagrams of differences in SST anomalies from Day -30 to Day 30 according to **a** the green triangle in Fig. 6b (one example of CIO mode positive peak on Aug. 22nd, 2004) and **b** all the red and blue circles in Fig. 6a–c. The composites are averaged between 2°N to 2°S . The white crosses represent the “centroid” of temperature anomaly at each longitude from Day -10 to Day 10 . The black solid lines in **(a)** and **(b)** are the estimated least square fit. The slope for **a** is around -0.19 day/degree and for **b** is around -0.16 day/degree



The mean intraseasonal SST differences between the peaks (days with red circles in Fig. 6a–c) and the troughs (days with blue circles in Fig. 6a–c) are shown in Fig. 6d. Warm SST anomalies over the tropical Indian Ocean (from 70°E to the western coast of Sumatra) are around 0.2°C which is consistent with their amplitude in observations (Schott et al. 2009; Shinoda et al. 1998). In addition, SST differences from central to eastern tropical Indian Ocean are statistically significant at 95% confidence level, which is a reliable depiction of the observed intraseasonal SST anomalies associated with the CIO mode in the tropics (between 5°N and 5°S in Fig. 1a). There are also significant negative SST differences over the northern and central BoB, which is consistent with the SST anomalies in the same region in Fig. 1a. However, it is surmised that the SST anomalies over the northern BoB are not solely attributable to the ocean dynamics. Air-sea interactions associated with atmospheric dynamics (such as MISO) and ocean–atmosphere coupling should also play a role. We intend to restrict this study to ocean dynamics alone. Variabilities over the northern BoB will be explored and reported separately (also see Xi et al. 2015).

The westward propagation of intraseasonal SST anomalies is shown in Fig. 7. Figure 7a displays the westward propagation around 22nd Aug 2004, and Fig. 7b shows the composite of all selected cases. The westward propagation speed is around 0.19 degree/day in Fig. 7a and is about 0.16 degree/day in Fig. 7b, both of which agree with observations (Fig. 3). However, the westward-propagating warm SST anomalies in ECCO2 only reach till

around 85°E . In contrast, the western edge in observations is at about 70°E (colors in Fig. 3). Such a bias should not qualitatively affect the investigation into the mechanism of oceanic ISVs over the tropical Indian Ocean but may have impacts on the analyses of their maintenance and propagation. Thus, in Sects. 4.3 and 4.4, various observations are also employed to verify the robustness of the conclusions which are drawn mainly based on the reanalysis products.

4.2 Budget analysis of the surface mixed layer

A heat budget analysis is conducted following Eq. (2) using ECCO2. Composite Hovmöller diagrams for all terms in the heat budget with respect to Day 0 (the days marked with red circles in Fig. 6a–c) are shown in Fig. 8 (colors), superimposed with the composite intraseasonal SST anomalies (contours) which are also shown in Fig. 7b. The net heat gain in the mixed layer (Q' ; the sum of latent heat flux, sensible heat flux, longwave radiation, shortwave radiation, and penetrative radiation) is an important component (Fig. 8e). Starting from Day -18 , positive Q' anomalies occur across the tropical Indian Ocean from 75°E to 100°E . As a result, warm intraseasonal SST anomalies occur through the tropical Indian Ocean around Day -10 (black contours in Fig. 8e). This is consistent with the CIO mode structure (Fig. 11 in Zhou et al. 2017b) in that a subsidence enhances the solar radiation and contributes to warm SST anomalies over the tropical Indian Ocean. However, warm SST anomalies around Day -10 are about 0.1°C , while the maximum SST anomaly is about 0.4°C (on Day 0 near 90°E), which agrees

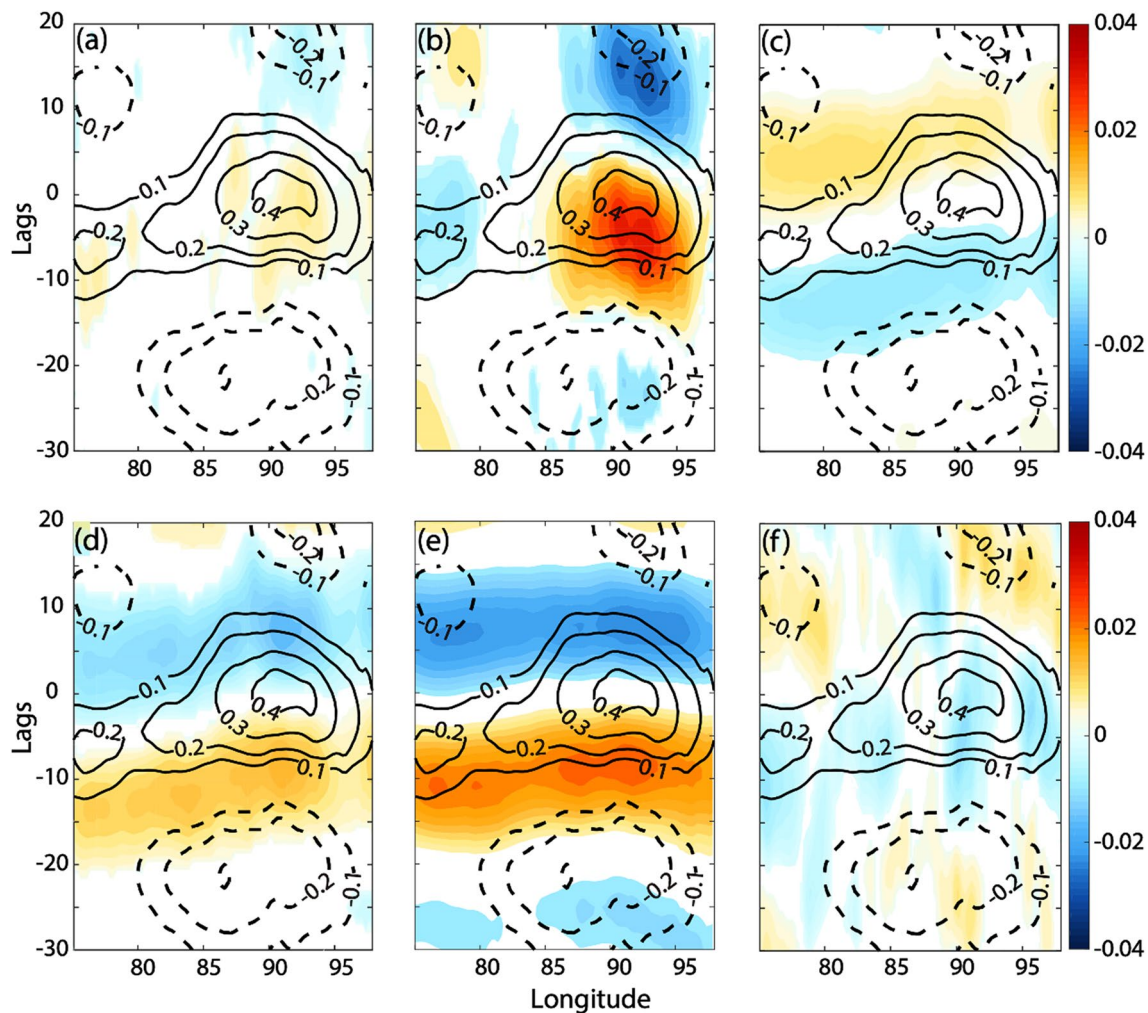


Fig. 8 Composite Hovmöller diagrams of all terms in Eq. (2) from Day -30 to Day 20 , which are averaged from 2°N to 2°S . Day 0 are the days marked with red circles in Fig. 3a. **a** is for $adv\overline{U'T'}$, **b** for $advU'T'$, **c** for V'_{adv} , **d** for Ent' , **e** for $\frac{Q'}{\rho c_p h}$ and **f** for $\langle R_H \rangle'$. Black contours in each panel are the composite intraseasonal SST anomalies.

The unit is $^{\circ}\text{C}/\text{day}$ for heat budget terms and $^{\circ}\text{C}$ for SST. All signals shown are statistically significant at a 95% confidence level

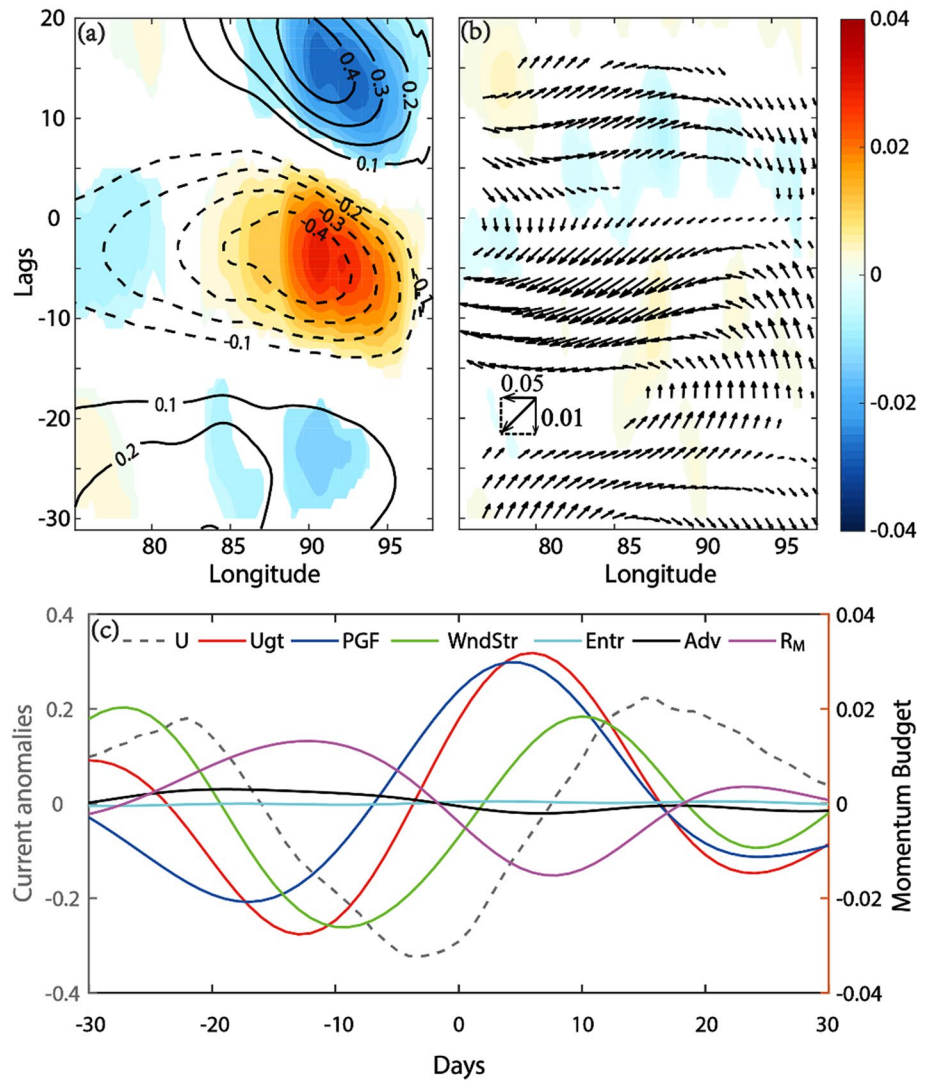
with the fact that Q' only explains about 30% of intraseasonal SST variance associated with the CIO mode as shown in Fig. 5. Moreover, Q' does not propagate westward (reddish colors in Fig. 8e) and it cannot explain the westward propagation of warm SST anomalies from 100°E to 85°E (solid contours). Therefore, we reiterate that while net heat flux term is important, it is not a dominant term in the heat budget (Seiki et al. 2013).

For horizontal advection, the background SST advected by the intraseasonal currents ($advU'T'$; colors in Fig. 8b) overwhelms all other terms in the heat budget, but $adv\overline{U'T'}$ (colors in Fig. 8a) is weak. During a positive CIO mode, $advU'T'$ becomes significantly positive (reddish in Fig. 8b) in the eastern Indian Ocean at 95°E around Day -15 . Then, positive $advU'T'$ propagates westward and reaches

85°E around Day 5, which is coherent with the westward propagation of intraseasonal SST anomalies (solid contours in Fig. 8b) from 100°E to 85°E and leads the SST anomalies by about 5 days. $advU'T'$ can be further decomposed into the zonal component ($-\langle u' \frac{\partial \overline{T}}{\partial x} \rangle$) and the meridional component ($-\langle v' \frac{\partial \overline{T}}{\partial y} \rangle$). As shown in Fig. 9a, b, $-\langle u' \frac{\partial \overline{T}}{\partial x} \rangle$ is the dominant component and $-\langle v' \frac{\partial \overline{T}}{\partial y} \rangle$ is negligible. The variation of u' (contours in Fig. 9a) within the upper mixed layer can be detected by a barotropic model of the shallow water system (Gill 2016). The zonal momentum budget is averaged within the upper mixed layer,

$$\frac{\partial u'}{\partial t} = Adv + Entr + PGF + WndStr + R_M, \quad (5)$$

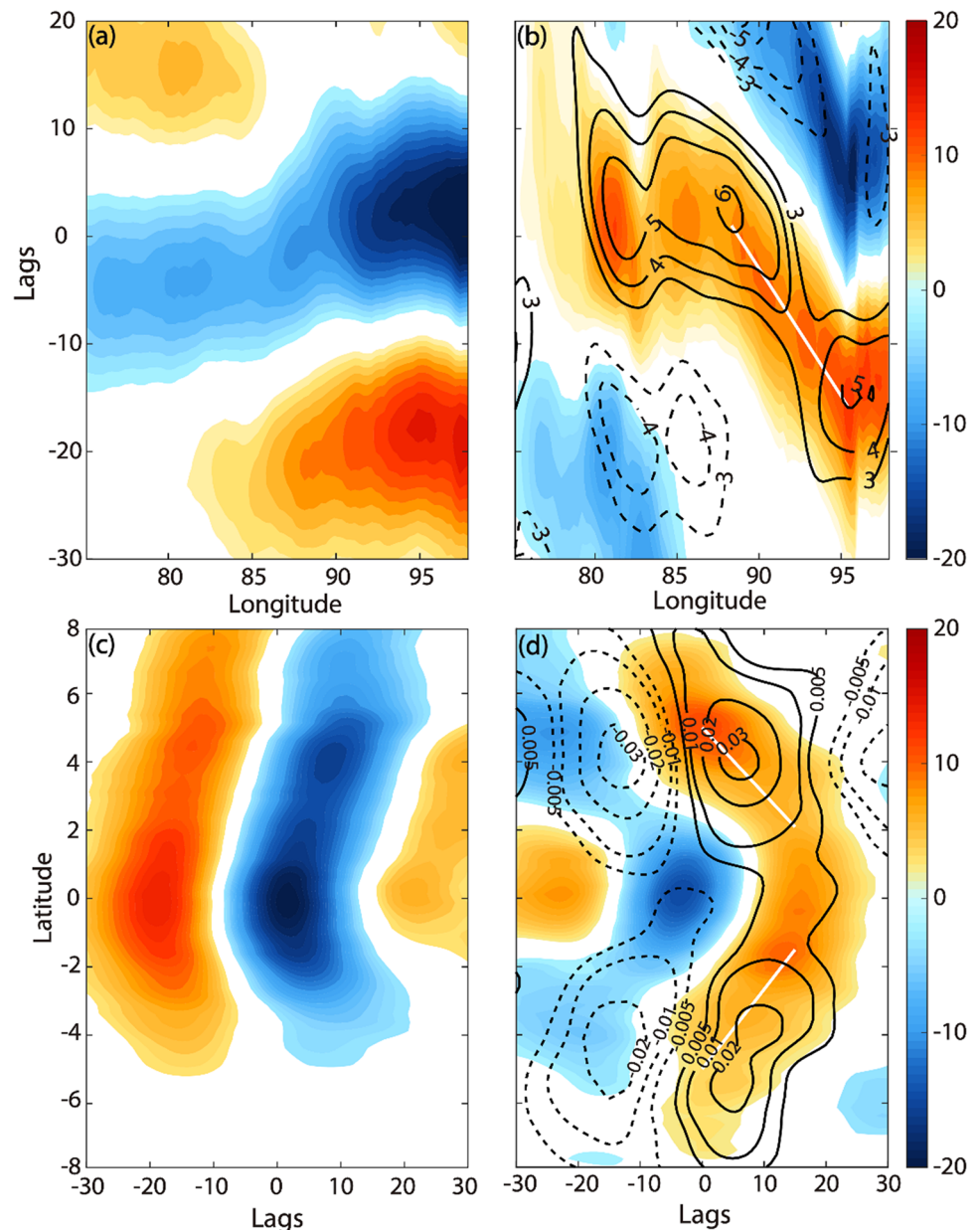
Fig. 9 **a** Colors are the same composite Hovmöller diagrams as in Fig. 8 but for $-\langle u' \frac{\partial T}{\partial x} \rangle$. Contours are the composite intraseasonal zonal currents (m/s). **b** Colors are the composite Hovmöller diagrams for $-\langle v' \frac{\partial T}{\partial y} \rangle$, vectors are composite intraseasonal wind stress anomalies (N/m^2). All signals shown are statistically significant at a 95% confidence level. **c** Composite zonal momentum budget (Eq. 5) averaged within 85°E – 100°E and 2°S – 2°N . The gray dashed line denotes $\langle u \rangle'$; the red line denotes $\frac{\partial \langle u \rangle'}{\partial t}$ (Ugt); the blue line denotes the pressure gradient force (PGF); the green line denotes the effect of wind stress (WndStr); the light blue line denotes the entrainment (Entr); the black line denotes the velocity advection (Adv; and the purple line denotes the residual term (R_M))



where $Adv = -\langle \bar{u} \cdot \nabla u \rangle'$ denotes the advection; $Entr = -\left(\frac{\langle u \rangle}{h} \frac{\partial h}{\partial t} - \frac{1}{h} \frac{\partial h}{\partial t} \cdot u|_{z=-h} \right)'$ denotes the momentum exchange due to entrainment; $PGF = -g \frac{\partial ssh'}{\partial x}$ denotes the effects from pressure gradient; $WndStr = \frac{1}{h} \frac{\Delta \tau'_x}{\rho}$ denotes the viscosity effect from the wind stress; R_M is the residual term. Within 85°E – 100°E and 2°S – 2°N , the changes in $\langle u \rangle'$ mainly come from the combined effects of pressure gradient force and wind stress (bluish and greenish in Fig. 9c). Around Day -15, the negative pressure gradient force and wind stress support the increasing westward ocean currents (reddish in Fig. 9c), which then make the term $-u' \frac{\partial T}{\partial x}$ positive and lead to positive tendency of $\langle T \rangle'$. Therefore, the westward propagation of intraseasonal SST anomalies in the tropics is mainly attributable to the zonal heat advection of mean temperature gradient by intraseasonal ocean currents. The intraseasonal currents themselves are driven by the negative pressure gradient and easterly wind stress associated with the positive CIO mode (Fig. 1a).

Besides the zonal advection and surface heat flux, entrainment (colors in Fig. 8d) is another discernible term in the heat budget. Entrainment has a clear eastward propagation (e.g., from 75°E on Day -18 to 100°E on Day -8). It is opposite to the westward propagation of intraseasonal SST anomalies within 85°E – 100°E (solid contours in Fig. 8d), but lines up with the eastward propagating SST within 75°E – 85°E . Vertical advection (colors in Fig. 8c) is a small term in the heat budget, but it also has an eastward propagation which is consistent with that of entrainment (e.g., from 75°E on Day -18 to 100°E on Day -8). Both entrainment and vertical advection are closely related to the intraseasonal MLD variabilities (h'). During a positive CIO mode, negative MLD anomalies propagate eastward from the central Indian Ocean ($\sim 75^\circ\text{E}$) around Day -15 to the eastern Indian Ocean at 100°E on Day 5 (bluish in Fig. 10a) at a speed of 2.6 m/s, which is consistent with the speed of the first baroclinic mode equatorial Kelvin waves. These MLD anomalies over eastern Indian Ocean

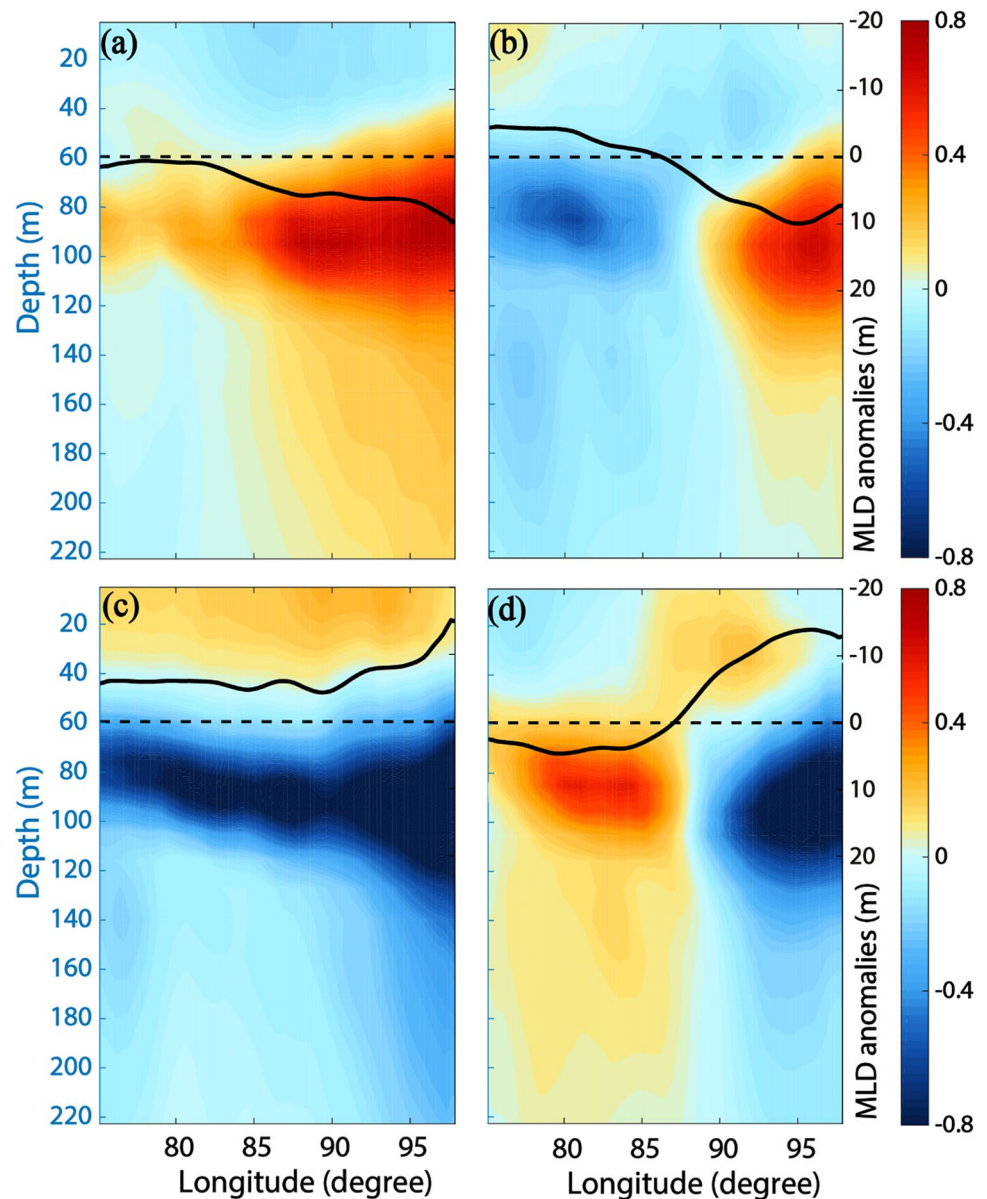
Fig. 10 Hovmöller diagram of intraseasonal MLD anomalies along: **a** the equator (averaged from 2°N to 2°S), **b** 5°N (colors; averaged from 4°N to 6°N) and 5°S (contours; averaged from 4°S to 6°S). Hovmöller diagram of intraseasonal MLD anomalies: **c** in the eastern Indian Ocean along 95°E (colors; averaged from 94°E to 96°E), **d** in the central Indian Ocean along 85°E (colors; averaged from 84°E to 86°E) and of observed intraseasonal SSH anomalies in the central Indian Ocean along 74°E (contours; averaged from 73°E to 75°E). The negative values of MLD denote a shallowing MLD. The white line in **b** is the ray trajectory of zonal signals starting from Day –15 and from 95°E, while those in **d** are meridional signals starting from Day 0 and from 5°N and 5°S, respectively. All signals shown are statistically significant at a 95% confidence level. The unit is meter



on Day –15 and Day 5 build up the MLD difference between the eastern and the central Indian Ocean (Fig. 10a). In the first baroclinic mode, comparable SSH anomalies between the eastern and the central Indian Ocean lead to the pressure gradient anomalies, then the westward propagation of temperature anomalies, as shown in Fig. 9. Moreover, variabilities beyond the deep tropics are also involved in the MLD changes during the CIO mode. The northward propagating coastal Kelvin waves are evident in the MLD anomalies at 95°E along the eastern boundaries of the Indian Ocean (bluish shade in Fig. 10c; also see Cheng et al. 2017). The southward propagating waves are also evident down to 5°S. The coastal Kelvin waves shed Rossby waves which propagate

westward at a speed of ~ 0.9 m/s along 5°N and 5°S, shown in the bluish color and dashed contours in Fig. 10b (same propagation as the red color and solid contours; also Cheng et al. 2017). Over the central Indian Ocean around 85°E, the convergence of the upwelling (downwelling) Rossby waves contribute to the shallowing (deepening) of MLD in the tropics on Day –10 (Day 10) during the positive (negative) CIO mode, as shown with the bluish (reddish) colors in Fig. 10d. The meridional propagation of energy can also be detected by the ray trajectory, i.e., $y = y_0 + c_{gy} * (t - t_0)$, where y_0 and t_0 refers to the start point and initial time of the meridional propagation. The meridional group velocity is $c_{gy} = \frac{\partial \omega}{\partial k_y} = \frac{2\beta k_x k_y}{[(k_x^2 + k_y^2) + R_d^{-2}]^2}$

Fig. 11 Composite longitude-depth profiles of intraseasonal temperature anomalies averaged between 2°N and 2°S on Day -26 (a), -13 (b), -5 (c), and 8 (d). Solid lines denote MLD anomalies. Dashed lines mark zero of MLD anomalies. The unit is °C for temperature anomalies and meter for MLD anomalies



(Cushman-Roisin and Beckers 2011; Pedlosky 1987), where β is the meridional gradient of Coriolis parameter; $k_x = 2.83 \times 10^{-6}$ rad/m is the zonal wavenumber and $k_y = 5.66 \times 10^{-6}$ rad/m is the meridional wavenumber, both of which are estimated based on Fig. 10; R_d is the Rossby radius of deformation which is estimated with the WKB method (Bender and Orszag 2013; Chelton et al. 1998). In Fig. 10d, the ray trajectories starting on Day 0 from 5°N and 5°S respectively are shown with the white lines. The zonal group velocity ($c_{gx} = \frac{\partial \omega}{\partial k_x} = \frac{\beta(k_x^2 - k_y^2 - R_d^{-2})}{[(k_x^2 + k_y^2) + R_d^{-2}]^2}$) along 5°N and 5°S is also calculated, and the associated ray trajectory is shown as a white line in Fig. 10b. These trajectories are consistent with the MLD anomalies (colors in Fig. 10b, d).

These MLD signals are also obvious in SSH, which is consistent with the first baroclinic mode (Gnanaseelan and Vaid 2010; Gnanaseelan et al. 2008). The observational convergence of Rossby waves from AVISO SSH data occurs around 74°E (black contours in Fig. 10d), which is consistent with the difference between ECCO2 and observations as illustrated in Fig. 3. The impacts of these equatorial waves in the deep tropics are consistent with the altimeter observations (such as Fig. 4a in Chelton and Schlax 1996) and results of ocean heat content (OHC) analyses in Rydbeck et al. (2019).

The residual term in the heat budget is not large (colors in Fig. 8f) indicating that the resolved terms in the heat budget using ECCO2 are largely balanced.

Vertical profiles of the composite intraseasonal temperature anomalies (averaged between 2°N and 2°S) are shown in Fig. 11. On Day -26 of the negative CIO mode (Fig. 11a), negative SST anomalies occupy the tropical Indian Ocean from 75°E to 100°E, which is again mainly attributable to zonal advection, $-u' \frac{\partial \bar{T}}{\partial x}$ (Fig. 9a). The reduced surface heat flux plays a secondary role compared with the zonal advection, as shown in Fig. 8b, e. In this phase, MLD (solid lines in Fig. 11a) is deeper than climatology (dashed lines in Fig. 11) from the central to the eastern Indian Ocean. In about a quarter cycle, on Day -13 (Fig. 11b), MLD anomalies over the central Indian Ocean (~80°E) become negative due to the influence of upwelling Rossby waves (dashed contours in Fig. 10b). But as mentioned above, since free Rossby waves are not clearly seen over the equator, these signals cannot propagate westward. They are instead forced to propagate eastward as equatorial Kelvin waves as shown in the Hovmöller diagram in Fig. 10a (bluish). It seems that there is a conversion from the Rossby waves to the Kelvin waves. There should be a mechanism for the conversion between the two kinds of waves around the tropical Indian Ocean. Although the evidence is distinct, the mechanism is still an open question which requires further studies in tropical wave dynamics. Due to a shallow MLD in the central Indian Ocean, cold anomalies occur below MLD around 80°E at 85 m on Day -13 (Fig. 11b). Meanwhile, deep MLD anomalies and warm temperature anomalies below the MLD (85 m) persist in the eastern tropical Indian Ocean (~95°E). On Day -5 (Fig. 11c), during the positive CIO mode, warm SST anomalies occur over the tropical Indian Ocean, which is again mainly attributable to the zonal advection ($-u' \frac{\partial \bar{T}}{\partial x}$; Fig. 9a) driven by the easterly wind anomalies. As a result, the warm SST anomalies propagate westward from 100°E to 85°E in ECCO2 (colors in Fig. 7b). At the same time, negative MLD anomalies starting from the central Indian Ocean on Day -13 (Fig. 11b) reach the eastern Indian Ocean (~100°E; bluish around Day -5 in Fig. 10a) and the MLD is shallower (solid line in Fig. 11c) than its climatology (dashed line in Fig. 11c) throughout the tropical Indian Ocean. Correspondingly, there are cold temperature anomalies below the MLD (bluish around 85 m in Fig. 11c), which is opposite to Fig. 11a. In another quarter cycle, on Day 8, MLD (solid line) becomes deeper over the central Indian Ocean around 80°E (Fig. 11d) due to downwelling Rossby waves (reddish in Fig. 10d), but it remains negative in the eastern Indian Ocean (~100°E; Fig. 11d). As a result, around the bottom of the MLD at about 85 m, there are warm anomalies in the central Indian Ocean, but cold anomalies in the eastern Indian Ocean, which is an opposite pattern to the one on Day -13 in Fig. 11b. Positive MLD perturbations starting from the central Indian Ocean also propagate eastward along the equator as Kelvin waves. Then, the composite cycle is closed by going back to Fig. 11a.

Overall, temperature and MLD anomalies shown in Fig. 11 illustrate an oscillatory cycle in the longitude-depth plane.

4.3 Three-dimensional structure of oceanic ISVs

Based on the results from ECCO2, a three-dimensional dynamics framework over the tropical Indian Ocean can be summarized. In the sketch in Fig. 12, the central Indian Ocean refers to the tropical region around 70°E. However, due to biases in ECCO2, evidence for the variabilities is shown around 85°E in ECCO2. The eastern Indian Ocean refers to the tropical region off Sumatra around 100°E, which is consistent between observations and ECCO2. The major components in the three-dimensional dynamical cycle associated with the CIO mode are:

- (1) Zonal advection, $-\langle u' \frac{\partial \bar{T}}{\partial x} \rangle$, is the dominant component in the surface mixed layer heat budget and it leads to the westward propagation of intraseasonal SST anomalies from the eastern to the central Indian Ocean;
- (2) MLD anomalies due to upwelling/downwelling Rossby waves originate in the central Indian Ocean, and are forced to propagate eastward as the equatorial Kelvin waves to the eastern Indian Ocean;
- (3) Entrainment and MLD anomalies in both central and eastern Indian Ocean are an integral component for intraseasonal SST variabilities, but not a dominant one.

The dominance of zonal advection in the heat budget is distinct from the atmosphere-forced oceanic ISVs (like the MJO-forced ocean response). Using data from RAMA array and Argo, 23 CIO mode events are selected to verify the effects from temperature advection. The peak days of the 23 CIO mode events are marked with black plus signs in Fig. 6a–c and listed in Table 1. Note that the 23 CIO mode events listed in Table 1 are based on actual CIO mode index (Fig. 6a–c). The locations of the Argo floats near the RAMA array during the 23 CIO mode events are shown in Fig. 13. The heat budget terms at the RAMA array (0°, 90°E) are estimated using in-situ data following Eq. (2) (see details in Sect. 2.2). If there are more than one Argo profiles available during one event (for ex., there are 3 Argo profiles available for Event #1; Fig. 13), the heat budget components are calculated using each Argo profile and then an average of all results is taken. Such a procedure helps to reduce the uncertainty of the results. For each event, all terms are calculated as the mean from 10 days before to 10 days after the peak days, and the results are shown in Fig. 14. For example, for Event #1 with a peak day on June 18th, 2004 (Table 1), the average is from Jun 8th, 2004 to Jun 28th, 2004. In 23 events listed in Table 1, $-\langle u' \frac{\partial \bar{T}}{\partial x} \rangle$ are all positive, which confirms that the westward advection leads to warm SST tendency over

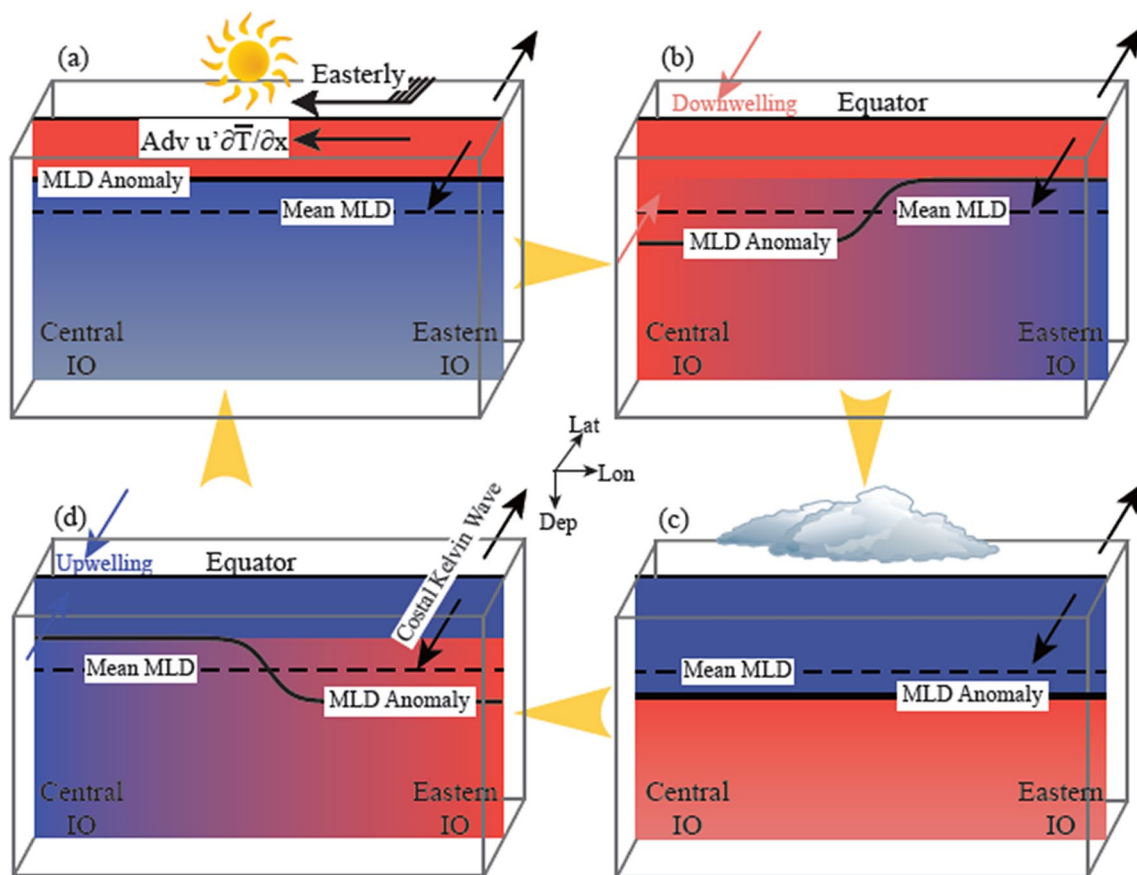


Fig. 12 Dynamical cycle for the oceanic ISVs associated with the CIO mode. Reddish colors denote warm anomalies and bluish colors denote cold anomalies. Dashed lines denote the change of background MLD, while black solid lines denote the intraseasonal MLD

anomalies. Arrows denote the convergence and divergence occurring in the central and the eastern Indian ocean, in which red and blue arrows denote the convergence produced by downwelling and upwelling Rossby waves

Table 1 The days with the maximum CIO mode index in 23 events from 2004 to 2017

| Event no. | Date | Event no. | Date |
|-----------|-----------|-----------|-----------|
| 1 | 2004/6/18 | 13 | 2010/8/2 |
| 2 | 2004/8/22 | 14 | 2010/9/1 |
| 3 | 2005/7/31 | 15 | 2011/6/18 |
| 4 | 2005/9/16 | 16 | 2011/9/2 |
| 5 | 2006/8/11 | 17 | 2011/9/24 |
| 6 | 2006/9/30 | 18 | 2013/6/16 |
| 7 | 2007/7/8 | 19 | 2013/7/26 |
| 8 | 2007/8/8 | 20 | 2013/9/21 |
| 9 | 2007/9/28 | 21 | 2015/7/11 |
| 10 | 2008/6/17 | 22 | 2015/9/18 |
| 11 | 2008/8/3 | 23 | 2017/9/22 |
| 12 | 2008/9/19 | | |

The days are also marked with black plus signs in Fig. 6a–c. These cases are used for observed validation in Figs. 13, 14, 15. The selection of these cases basically refers to the availability of RAMA array at (0°, 90°E) and the surrounding Argo floats, which extends from 2004 to 2017

the central Indian Ocean. In addition, $-\langle u' \frac{\partial \bar{T}}{\partial x} \rangle$ is the largest advection term in 16 of the 23 events. And in 20 of 23 events, $-\langle u' \frac{\partial \bar{T}}{\partial x} \rangle$ is larger than or at least comparable with $\frac{Q'}{\rho C_p h}$. An average of these events shows that $-\langle u' \frac{\partial \bar{T}}{\partial x} \rangle$ dominates the mean heat budget (gray colors in Fig. 14). Therefore, the estimates based on RAMA array and Argo data, despite the data limitations, are consistent with the conclusions obtained from ECCO2 that the zonal advection $-\langle u' \frac{\partial \bar{T}}{\partial x} \rangle$ driven by pressure gradient and easterly wind anomalies is mainly responsible for the westward propagation of warm intraseasonal SST anomalies in the tropical Indian Ocean.

4.4 Possible enhancement of ocean mixing over the central Indian Ocean

The deepening of MLD over the central Indian Ocean during the positive CIO mode (Fig. 12b) is a distinct feature during the Indian summer monsoon. It may be attributed to the

Fig. 13 Locations of Argo profiles used to evaluate the advection components in the heat budget for each CIO mode event listed in Table 1. For each event, all available Argo profiles (different signs in the same color) are averaged, which helps to reduce the randomness of the evaluation. The black triangle marks the position of the RAMA buoy at (0°, 90°E). The gray patches are the land

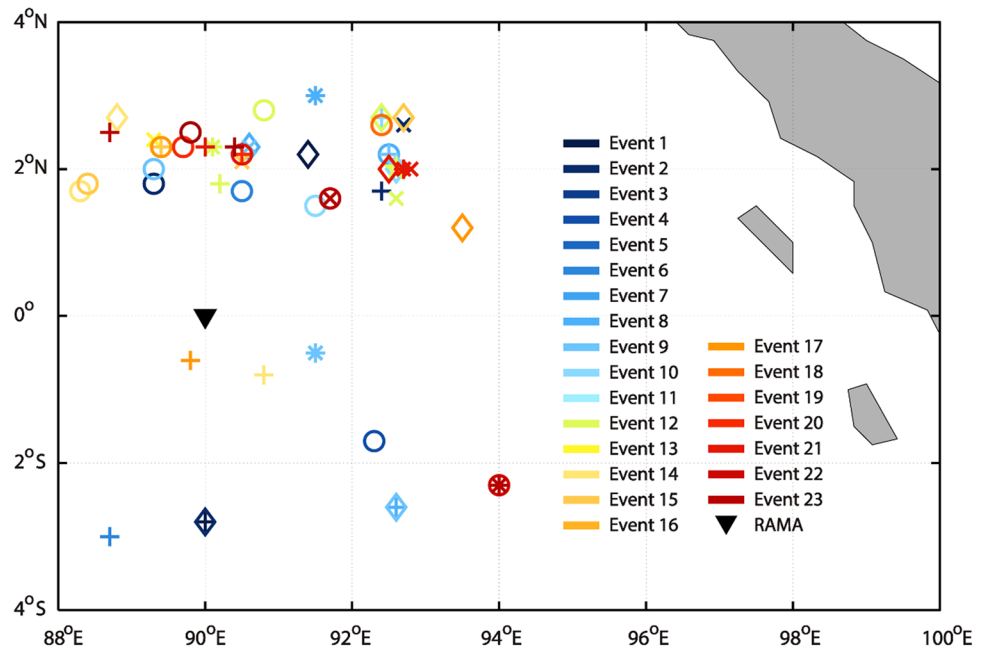
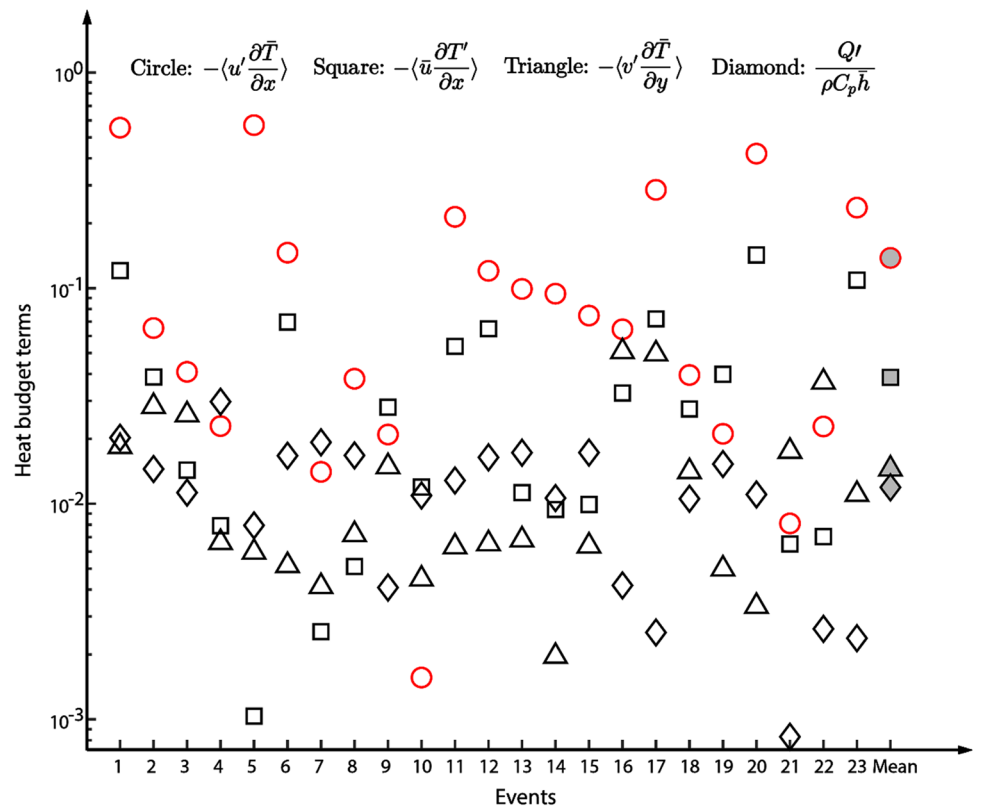


Fig. 14 Major heat budget terms in Eq. (2) estimated using RAMA, Argo, and TropFlux. All results are averaged between 10 days before and 10 days after the days with maximum CIO mode indices listed in Table 1. The units are °C/day. The symbols filled with gray color denote the mean of the 23 events

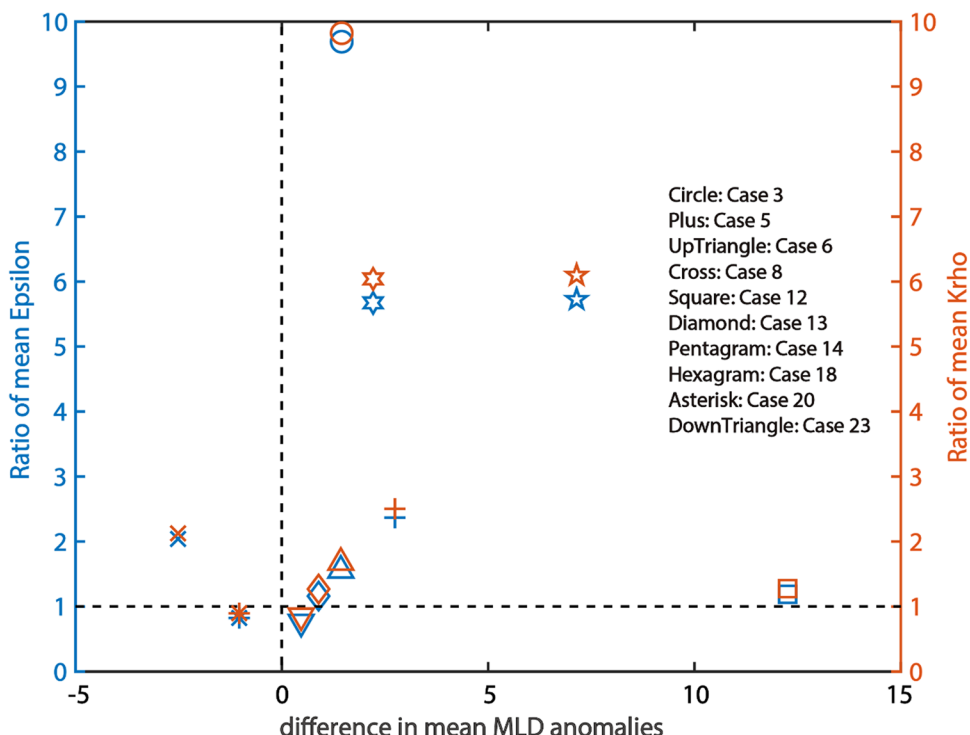


influence of downwelling Kelvin waves as discussed above (solid contours in Fig. 10a).

Nevertheless, another possible mechanism is ocean mixing. Around 90°E, stronger stratification due to large salinity in the vertical leads to a barrier layer and accounts for weaker subsurface turbulent mixing than those at 80°E, as

discussed in Pujiana and McPhaden (2018). The observed zonal variation of ocean mixing across the equatorial Indian Ocean is consistent in Fig. 11c, d showing that entrainment is more pronounced at 80°E than 90°E. The enhanced mixing helps to deepen and cool the upper mixed layer, since it carries warm water from the upper mixed layer down to the

Fig. 15 Ratios of energy dissipation (left vertical axis) and mixing ratio (right vertical axis) between the mean of Day 0–5 and the mean of Day 5–10 for 10 CIO mode events in Table 1. The horizontal axis is the corresponding MLD differences between the mean of Day 0–5 and the mean of Day 5–10. The unit for MLD is m



ocean interior and brings cold water from ocean interior up to the surface layer. As a result, cold anomalies occur in the surface layer (bluish in Fig. 11d around 80°E) and warm anomalies occur below the MLD (reddish in Fig. 11d around 80°E). Meanwhile, MLD becomes deeper over the central Indian Ocean (solid line in Fig. 11d). The details for ocean mixing cannot be examined using reanalysis products, as they do not provide the needed parameters. However, it can be implied with in-situ observations (Pujiana et al. 2018). Using Argo profiles, the mixing ratio can be approximately estimated in the upper ocean following the Gregg–Henyey–Polzin (GHP) scaling (Gregg et al. 2003). The turbulent kinetic energy dissipation rate is calculated as $\epsilon = \epsilon_0 \frac{N^2 \langle \xi^2 \rangle^2}{N^2 \langle \xi^2 \rangle_{GM}^2} h_2(R_\omega) j\left(\frac{f}{N}\right)$, where $\epsilon_0 = 6.73 \times 10^{-10}$ W/kg, f is the Coriolis parameter, N is the Brunt–Väisälä frequency (Kunze et al. 2006), $\langle \xi^2 \rangle^2$ and $\langle \xi^2 \rangle_{GM}^2$ denote the fine-scale strain variance inferred from observations and the Garrett and Munk (GM) spectrum (Garrett and Munk 1972, 1975). $R_\omega = 7$ represents the shear-to-strain variance ratio and h_2 is a function of R_ω (see Kunze et al. 2006 for the explicit form). The function $j\left(\frac{f}{N}\right)$ represents the latitude dependence of the scaling. Then, the mixing rate is $\kappa_p = 0.2 \frac{\epsilon}{N^2}$ (Osborn 1980), where 0.2 is the value of mixing efficiency. Argo profiles exist in the equatorial Indian Ocean (within 3°N–3°S and 78°E–85°E) for 10 CIO mode events (Event # 3, 5, 6, 8, 12, 13, 14, 18, 20 and 23 in Table 1). If more than one Argo profile is available for an event, the average of all available Argo profiles is taken, which reduces the randomness of the

results. As shown in Fig. 14, after the peak of the positive CIO mode (average between Day 0 and Day 5 with respect to the peak days in Table 1), the mean energy dissipation and the mean mixing ratio in the upper ocean are enhanced in 7 out of 10 events, i.e., Event # 3, 5, 6, 12, 13, 14 and 18. As a result, MLD becomes deeper right after the warm SST anomalies occur during the positive CIO mode as shown in Fig. 10d. A caveat is that the GHP scaling was designed for the mixing due to internal wave breaking in the ocean interior. It is not fully applicable to the tropical region in the upper layer. However, the consistent mixing reinforcement in a number of CIO mode events affirms the robustness of the phenomena (Pujiana et al. 2018), although there can be considerable uncertainty. The exact mechanism for the enhanced mixing over the central Indian Ocean is of interest for further field observations and analyses.

5 Conclusions and discussion

The CIO mode has been shown to play an important role in the northward-propagating MISO and the enhancement of the ISVs during the Indian summer monsoon. The phenomenon of the CIO mode and its dynamics in the atmosphere were discussed in previous studies (Zhou et al. 2017a, b, 2018). In this study, the ocean dynamics associated with the CIO mode in the tropical Indian Ocean are analyzed using reanalysis products, satellite data, and in-situ observations. The intraseasonal SST anomalies over the tropical Indian

Ocean have different features from the traditional ones, which are attributed to the ocean responses to the MJO. Particularly, intraseasonal SST anomalies propagate westward along the equator, which is distinct from either the equatorial Kelvin waves or the MJO. According to the heat budget analysis, zonal advection $-\langle u' \frac{\partial T}{\partial x} \rangle$ is the dominant component for the intraseasonal SST variabilities during the CIO mode. Surface heat flux only accounts for about 30% of the intraseasonal SST variance. In addition, entrainment is also important along with the MLD changes which propagate eastward as equatorial Kelvin waves from central to eastern Indian Ocean. A framework for the three-dimensional ocean dynamics is summarized in Fig. 12.

Current results unveil a different dynamic regime for the oceanic ISVs over the tropical Indian Ocean from the traditional ocean responses to the MJO. Surface heat flux changes due to atmospheric forcing are not the dominant control for the tropical oceanic ISVs associated with the CIO mode. Instead, the ocean dynamics play an active role and control the ISVs in the tropical Indian Ocean. On the other hand, oceanic ISVs, particularly intraseasonal SST variabilities, can feedback to the atmosphere, which leaves clear fingerprints on the atmospheric ISVs, such as MJO and MISO. In fact, the oceanic impacts on MJO and MISO are receiving more and more attention (e.g., Annamalai and Sperber 2005; Vecchi and Harrison 2002; Xi et al. 2015; Zhou and Murtugudde 2014 and many others). The current study reinforces the importance of ocean dynamics in the weather and climate system over the Indian Ocean. Therefore, in order to have a better simulation and forecast of the weather and climate over the Indian Ocean (such as MISO and Indian monsoon), a full ocean model is clearly a necessary component, to capture the detailed three-dimensional ocean dynamics presented in this study. The intricate role played by the eastern Indian Ocean during boreal summer is posited to be critical for the multi-scale interactions between the ITCZ, monsoon dynamics and MISOs which is encapsulated in the rather complex ocean dynamics discussed here (Murtugudde 2021).

A caveat of this study is the limited ability of ocean reanalysis products to fully capture the observed ISVs. Comprehensive comparisons are conducted between various reanalysis products, and the results confirm that ECCO2 has the best ability to capture the ISVs and the CIO mode. Moreover, a lot of care is taken to empirically select the CIO mode events which are comparable to observations. However, a day-to-day match between the state-of-the-art reanalysis products and observations is still poor. Thus, carefully designed observations are required to have a better understanding and a more accurate reproduction

of the ocean dynamics during the CIO mode. For example, the westward-propagating SST anomalies only reach up to 85°E in ECCO2 while they reach further to 70°E in observations. In the meantime, the MISO simulation and monsoon forecast still remain serious scientific challenges (Hurley and Boos 2013; Li et al. 2016; Wang et al. 2015; Qin et al. 2020, etc.). As shown in Zhou et al. (2018) using various Community Earth System Model (CESM) simulations, a better CIO mode simulation facilitated the improvement of MISO and ISVs during the Indian summer monsoon. However, the forcing-and-response relation in CESM between the ocean and the atmosphere is opposite to that in observations, which is likely to be partly attributable to the poor representation of the ocean dynamics associated with the CIO mode. Therefore, more modelling studies are called for to improve the simulation of the CIO mode in the couple ocean-atmosphere models, which will ultimately contribute to improving monsoon simulations, predictions and projections.

Appendix

The thermodynamic equation for the ocean can be written as

$$\frac{\partial T}{\partial t} = -\vec{U}_H \cdot \nabla_H T - w \frac{\partial T}{\partial z} + \frac{1}{\rho C_p} \frac{\partial Q}{\partial z} + R, \quad (6)$$

where T is the temperature; $\vec{U}_H = \vec{u}\vec{i} + \vec{v}\vec{j}$ is the horizontal velocity vector, \vec{i} and \vec{j} are the unit vectors in the eastward and northward directions, respectively; $\nabla_H = \frac{\partial}{\partial x}\vec{i} + \frac{\partial}{\partial y}\vec{j}$; w is the vertical velocity; Q is diabatic heating, C_p is the heat capacity, and ρ is the seawater density; R denotes the residuals which also includes the unresolved eddy diffusivity. Define the vertical mean in the upper mixed layer, $\langle \rangle = \frac{1}{h} \int_{-h}^0 dz$, where h is the MLD. And $\langle \frac{1}{\rho C_p} \frac{\partial Q}{\partial z} \rangle \approx \frac{Q}{\rho C_p h}$, where Q denotes the net surface heat flux retained in the upper mixed layer. Therefore,

$$\left\langle \frac{\partial T}{\partial t} \right\rangle = -\left\langle \vec{U}_H \cdot \nabla_H T \right\rangle - \left\langle w \frac{\partial T}{\partial z} \right\rangle + \frac{Q}{\rho C_p h} + \langle R \rangle. \quad (7)$$

Considering the MLD variation with time and positions and following the Leibniz's rule for the partial derivative of integral with variable limits, one has

$$\frac{\partial \langle T \rangle}{\partial t} = \left\langle \frac{\partial T}{\partial t} \right\rangle + \frac{1}{h} \frac{\partial h}{\partial t} (T|_{z=-h} - \langle T \rangle). \quad (8)$$

Substituting Eq. (7) into Eq. (8), one has

$$\frac{\partial \langle T \rangle}{\partial t} = - \left\langle \vec{U}_H \cdot \nabla_H T \right\rangle - \left\langle w \frac{\partial T}{\partial z} \right\rangle + \frac{1}{h} \frac{\partial h}{\partial t} (T|_{z=-h} - \langle T \rangle) + \frac{Q}{\rho C_p h} + \langle R \rangle. \quad (9)$$

which is Eq. (1) in the main text.

Acknowledgements This work is supported by grants from National Natural Science Foundation of China (42076001, 41690121, and 41690120), the China Ocean Mineral Resources Research and Development Association Program (DY135-E2-3-01, DY135-E2-3-05), Innovation Group Project of Southern Marine Science and Engineering Guangdong Laboratory (Zhuhai; 311020004), and the Oceanic Interdisciplinary Program of Shanghai Jiao Tong University (SL2020PT205). We acknowledge NOAA and its partners for maintaining the RAMA moored buoy array. RM gratefully acknowledges the Visiting Faculty position at the Indian Institute of Technology, Bombay. KP was supported by a National Research Council research associateship award at NOAA/PMEL. This is PMEL contribution 5044.

References

- Annamalai H, Sperber KR (2005) Regional heat sources and the active and break phases of boreal summer intraseasonal (30–50 day) variability. *J Atmos Sci* 62:2726–2748
- Argo (2000) Argo float data and metadata from Global Data Assembly Centre (Argo GDAC). SEANO
- Bender CM, Orszag SA (2013) Advanced mathematical methods for scientists and engineers I: asymptotic methods and perturbation theory. Springer Science & Business Media, Berlin
- Bretherton CS, Widmann M, Dymnikov VP, Wallace JM, Bladé I (1999) The effective number of spatial degrees of freedom of a time-varying field. *J Clim* 12:1990–2009
- Carton JA, Giese BS (2008) A reanalysis of ocean climate using Simple Ocean Data Assimilation (SODA). *Mon Wea Rev* 136:2999–3017
- Chelton DB, Schlax MG (1996) Global observations of oceanic Rossby waves. *Science* 272:234–238
- Chelton DB, DeSzoeka RA, Schlax MG, El Naggar K, Siwertz N (1998) Geographical variability of the first baroclinic Rossby radius of deformation. *J Phys Oceanogr* 28:433–460
- Cheng X, McCreary JP, Qiu B, Qi Y, Du Y (2017) Intraseasonal-to-semiannual variability of sea-surface height in the eastern, equatorial Indian Ocean and southern Bay of Bengal. *J Geophys Res Oceans* 122:4051–4067. <https://doi.org/10.1002/2016JC012662>
- Cushman-Roisin B, Beckers J-M (2011) Introduction to geophysical fluid dynamics: physical and numerical aspects. Academic Press, Cambridge
- de Szoeka SP, Edson JB, Marion JR, Fairall CW, Bariteau L (2015) The MJO and air-sea interaction in TOGA COARE and DYNAMO. *J Clim* 28:597–622
- Drushka K, Sprintall J, Gille ST (2014) Subseasonal variations in salinity and barrier-layer thickness in the eastern equatorial Indian Ocean. *J Geophys Res Oceans* 119:805–823
- Farrar JT, Durland TS (2012) Wavenumber–frequency spectra of inertia–gravity and mixed Rossby–gravity waves in the equatorial Pacific Ocean. *J Phys Oceanogr* 42:1859–1881
- Gill AE (2016) Atmosphere—ocean dynamics. Elsevier, Amsterdam
- Gnanaseelan C, Vaid BH (2010) Interannual variability in the Biannual Rossby waves in the tropical Indian Ocean and its relation to Indian Ocean Dipole and El Niño forcing. *Ocean Dyn* 60:27–40
- Gnanaseelan C, Vaid BH, Polito PS (2008) Impact of biannual Rossby waves on the Indian Ocean Dipole. *IEEE Geosci Remote Sens Lett* 5:427–429
- Goswami BN (2005) South Asian monsoon. Intraseasonal variability in the atmosphere–ocean climate system. Springer, Berlin, pp 19–61
- Gregg MC, Sanford TB, Winkel DP (2003) Reduced mixing from the breaking of internal waves in equatorial waters. *Nature* 422:513–515
- Hendon HH (2003) Indonesian rainfall variability: impacts of ENSO and local air-sea interaction. *J Clim* 16:1775–1790
- Hendon HH, Glick J (1997) Intraseasonal air–sea interaction in the tropical Indian and Pacific Oceans. *J Clim* 10:647–661
- Holte J, Talley LD, Gilson J, Roemmich D (2017) An Argo mixed layer climatology and database. *Geophys Res Lett* 44:5618–5626
- Hurley JV, Boos WR (2013) Thermodynamic bias in the multimodel mean boreal summer monsoon*. *J Clim* 26:2279–2287
- Jiang X, Li T, Wang B (2004) Structures and mechanisms of the northward propagating boreal summer intraseasonal oscillation. *J Clim* 17:1022–1039
- Jiang X et al (2015) Vertical structure and physical processes of the Madden-Julian oscillation: exploring key model physics in climate simulations. *J Geophys Res Atmos* 120:4718–4748
- Jin D, Waliser DE, Jones C, Murtugudde R (2012) Modulation of tropical ocean surface chlorophyll by the Madden–Julian Oscillation. *Clim Dyn* 40:39–58
- Jin D, Murtugudde RG, Waliser DE (2013) Intraseasonal atmospheric forcing effects on the mean state of ocean surface chlorophyll. *J Geophys Res Oceans* 118:184–196
- Kang I-S, Kim D, Kug J-S (2010) Mechanism for northward propagation of boreal summer intraseasonal oscillation: convective momentum transport. *Geophys Res Lett* 37:L24804. <https://doi.org/10.1029/2010GL045072>
- Kara AB, Rochford PA, Hurlburt HE (2000) An optimal definition for ocean mixed layer depth. *J Geophys Res* 105:16803–16821
- Kiladis GN, Straub KH, Haertel PT (2005) Zonal and vertical structure of the Madden-Julian oscillation. *J Atmos Sci* 62:2790–2809
- Kumar BP, Vialard J, Lengaigne M, Murty VSN, McPhaden MJ (2012) TropFlux: air-sea fluxes for the global tropical oceans—description and evaluation. *Clim Dyn* 38:1521–1543
- Kunze E, Firing E, Hummon JM, Chereskin TK, Thurnherr AM (2006) Global abyssal mixing inferred from lowered ADCP shear and CTD strain profiles. *J Phys Oceanogr* 36:1553–1576
- Li X, Tang Y, Zhou L, Chen D, Yao Z, Islam SU (2016) Assessment of Madden-Julian oscillation simulations with various configurations of CESM. *Clim Dyn* 47:2667–2690
- Li B, Zhou L, Wang C, Gao C, Qin J, Meng Z (2020) Modulation of tropical cyclone genesis in the Bay of Bengal by the Central Indian Ocean Mode. *J Geophys Res Atmos* 125:e2020JD032641
- Masumoto Y, Hase H, Kuroda Y, Matsuura H, Takeuchi K (2005) Intraseasonal variability in the upper layer currents observed in the eastern equatorial Indian Ocean. *Geophys Res Lett* 32:L02607. <https://doi.org/10.1029/2004GL021896>
- McPhaden MJ et al (2009) RAMA: the research moored array for African–Asian–Australian monsoon analysis and prediction*. *Bull Am Meteorol Soc* 90:459–480
- Menemenlis D et al (2005) NASA supercomputer improves prospects for ocean climate research. *EOS Trans Am Geophys Union* 86:89–96
- Monterey GI, Levitus S (1997) Seasonal variability of mixed layer depth for the world ocean. US Department of Commerce, National Oceanic and Atmospheric Administration, National Environmental Satellite, Data, and Information Service
- Murtugudde R, Busalacchi AJ (1999) Interannual variability of the dynamics and thermodynamics of the tropical Indian Ocean. *J Clim* 12:2300–2326

- Murtugudde R (2021) Indian Summer Monsoon System: a holistic approach for advancing monsoon understanding in a warming world. *Hydrological Aspects of Climate Change*, p 77
- Nagura M, McPhaden MJ (2010) Wyrтки jet dynamics: seasonal variability. *J Geophys Res* 115:C07009. <https://doi.org/10.1029/2009JC005922>
- Osborn TR (1980) Estimates of the local rate of vertical diffusion from dissipation measurements. *J Phys Oceanogr* 10:83–89
- Paulson CA, Simpson JJ (1977) Irradiance measurements in the upper ocean. *J Phys Oceanogr* 7:952–956
- Pedlosky J (1987) *Geophysical fluid dynamics*, vol 710. Springer, Berlin
- Pujiana K, McPhaden MJ (2018) Ocean surface layer response to convectively coupled Kelvin waves in the eastern equatorial Indian Ocean. *J Geophys Res Oceans* 123:5727–5741
- Pujiana K, Moum JN, Smyth WD (2018) The role of turbulence in redistributing upper-ocean heat, freshwater, and momentum in response to the MJO in the Equatorial Indian Ocean. *J Phys Oceanogr* 48:197–220
- Qin J, Zhou L, Li B, Murtugudde R (2020) Simulation of Central Indian Ocean Mode in S2S models. *J Geophys Res Atmos* 125:e2020JD033550
- Qiu B, Miao W, Müller P (1997) Propagation and decay of forced and free baroclinic Rossby waves in off-equatorial oceans. *J Phys Oceanogr* 27:2405–2417
- Qu T (2003) Mixed layer heat balance in the western North Pacific. *J Geophys Res* 108:3242. <https://doi.org/10.1029/2002JC001536>
- Qu T, Meyers G (2005) Seasonal variation of barrier layer in the southeastern tropical Indian Ocean. *J Geophys Res* 110:C11003. <https://doi.org/10.1029/2004JC002816>
- Reynolds RW, Smith TM, Liu C, Chelton DB, Casey KS, Schlax MG (2007) Daily high-resolution-blended analyses for sea surface temperature. *J Clim* 20:5473–5496
- Rydbeck AV, Jensen TG, Smith TA, Flatau MK, Janiga MA, Reynolds CA, Ridout JA (2019) Ocean heat content and the intraseasonal oscillation. *Geophys Res Lett* 46:14558–14566
- Schott FA, Xie S-P, McCreary JP (2009) Indian Ocean circulation and climate variability. *Rev Geophys* 47:RG1002
- Seiki A, Katsumata M, Horii T, Hasegawa T, Richards KJ, Yoneyama K, Shirooka R (2013) Abrupt cooling associated with the oceanic Rossby wave and lateral advection during CINDY2011. *J Geophys Res Oceans* 118:5523–5535
- Shinoda T, Hendon HH, Glick J (1998) Intraseasonal variability of surface fluxes and sea surface temperature in the tropical western Pacific and Indian Oceans. *J Clim* 11:1685–1702
- Shinoda T, Kiladis GN, Roundy PE (2009) Statistical representation of equatorial waves and tropical instability waves in the Pacific Ocean. *Atmos Res* 94:37–44. <https://doi.org/10.1016/j.atmosres.2008.06.002>
- Stevenson JW, Niiler PP (1983) Upper ocean heat budget during the Hawaii-to-Tahiti Shuttle experiment. *J Phys Oceanogr* 13:1894–1907
- Vecchi GA, Harrison DE (2002) Monsoon Breaks and Subseasonal Sea Surface Temperature Variability in the Bay of Bengal*. *J Clim* 15:1485–1493
- Wakata Y (2007) Frequency-wavenumber spectra of equatorial waves detected from satellite altimeter data. *J Oceanogr* 63:483–490. <https://doi.org/10.1007/s10872-007-0043-4>
- Waliser DE (2006) *Intraseasonal variability. The Asian Monsoon*. Springer, Berlin, pp 203–257
- Waliser DE, Murtugudde R, Lucas LE (2003) Indo-Pacific Ocean response to atmospheric intraseasonal variability: 1. Austral summer and the Madden-Julian Oscillation. *J Geophys Res* 108:3160. <https://doi.org/10.1029/2002JC001620>
- Waliser DE, Murtugudde R, Lucas LE (2004) Indo-Pacific Ocean response to atmospheric intraseasonal variability: 2. Boreal summer and the Intraseasonal Oscillation. *J Geophys Res* 109:C03030. <https://doi.org/10.1029/2003JC002002>
- Wallace JM, Adames ÁF (2014) Three-dimensional structure and evolution of the MJO and its relation to the mean flow. *J Atmos Sci* 71:2007–2026
- Wang B, Ding Q, Fu X, Kang I-S, Jin K, Shukla J, Doblas-Reyes F (2005) Fundamental challenge in simulation and prediction of summer monsoon rainfall. *Geophys. Res Lett* 32:L15711. <https://doi.org/10.1029/2005GL022734>
- Wang B, Xiang B, Li J, Webster PJ, Rajeevan MN, Liu J, Ha KJ (2015) Rethinking Indian monsoon rainfall prediction in the context of recent global warming. *Nat Commun* 6:7154
- Weller RA, Yu L (2007) Objectively analyzed air-sea heat fluxes for the global ice-free oceans (1981–2005). *Bull Am Meteorol Soc* 88:527–540
- Wheeler MC, Hendon HH (2004) An all-season real-time multivariate MJO index: development of an index for monitoring and prediction. *Mon Weather Rev* 132:1917–1932
- Wyrтки K (1973) An equatorial jet in the Indian ocean. *Science* 181:262–264
- Xi J, Zhou L, Murtugudde R, Jiang L (2015) Impacts of intraseasonal SST anomalies on precipitation during Indian summer monsoon. *J Clim* 28:4561–4575
- Zhang M, Zhou L, Fu H, Jiang L, Zhang X (2016) Assessment of intraseasonal variabilities in China Ocean Reanalysis (CORA). *Acta Oceanol Sin* 35:90–101
- Zhang H-M, Bates JJ, Reynolds RW (2006) Assessment of composite global sampling: sea surface wind speed. *Geophys Res Lett* 33:L17714. <https://doi.org/10.1029/2006GL027086>
- Zhou L, Murtugudde R (2014) Impact of northward-propagating intraseasonal variability on the onset of Indian summer monsoon. *J Clim* 27:126–139
- Zhou L, Murtugudde R, Chen D, Tang Y (2017a) Seasonal and interannual variabilities of the central Indian Ocean mode. *J Clim* 30:6505–6520
- Zhou L, Murtugudde R, Chen D, Tang Y (2017b) A Central Indian Ocean mode and heavy precipitation during the Indian summer monsoon. *J Clim* 30:2055–2067
- Zhou L, Murtugudde R, Neale RB, Jochum M (2018) Simulation of the Central Indian Ocean mode in CESM: implications for the Indian summer monsoon system. *J Geophys Res Atmos* 123:58–72
- Zhou L, Sobel AH, Murtugudde R (2012) Kinetic energy budget for the Madden-Julian oscillation in a multiscale framework. *J Clim* 25:5386–5403

Publisher's Note Springer Nature remains neutral with regard to jurisdictional claims in published maps and institutional affiliations.